

Self supervised contrastive learning for digital histopathology

Ozan Ciga^{a,*}, Tony Xu^b, Anne L. Martel^{a,c}

^a*Department of Medical Biophysics, University of Toronto, Canada*

^b*Department of Electrical and Computer Engineering, University of British Columbia, Canada*

^c*Physical Sciences, Sunnybrook Research Institute, Toronto, Canada*

Abstract

Unsupervised learning has been a long-standing goal of machine learning and is especially important for medical image analysis, where the learning can compensate for the scarcity of labeled datasets. A promising subclass of unsupervised learning is self-supervised learning, which aims to learn salient features using the raw input as the learning signal. In this paper, we use a contrastive self-supervised learning method Chen et al. (2020a) that achieved state-of-the-art results on natural-scene images, and apply this method to digital histopathology by collecting and training on 60 histopathology datasets without any labels. We find that combining multiple multi-organ datasets with different types of staining and resolution properties improves the quality of the learned features. Furthermore, we find drastically subsampling a dataset (e.g., using \ll 1% of the available image patches) does not negatively impact the learned representations, unlike training on natural-scene images. Linear classifiers trained on top of the learned features show that networks pretrained on digital histopathology datasets perform better than ImageNet pretrained networks, boosting task performances up to 7.5% in accuracy and 8.9% in F_1 . These findings may also be useful when applying newer contrastive techniques to histopathology data. Pretrained PyTorch models are made publicly available at <https://github.com/ozanciga/self-supervised-histopathology>.

Keywords: Self supervised learning, digital histopathology, whole slide images, unsupervised learning

1. Introduction

The number of labeled images in machine learning tasks is found to be positively correlated with the task performance; however, labeled data is scarce and expensive. The problem is exacerbated in medical image analysis tasks, where expert annotations are required and crowdsourcing is not usually an option. In many

*Corresponding author: e-mail: ozan.ciga@mail.utoronto.ca

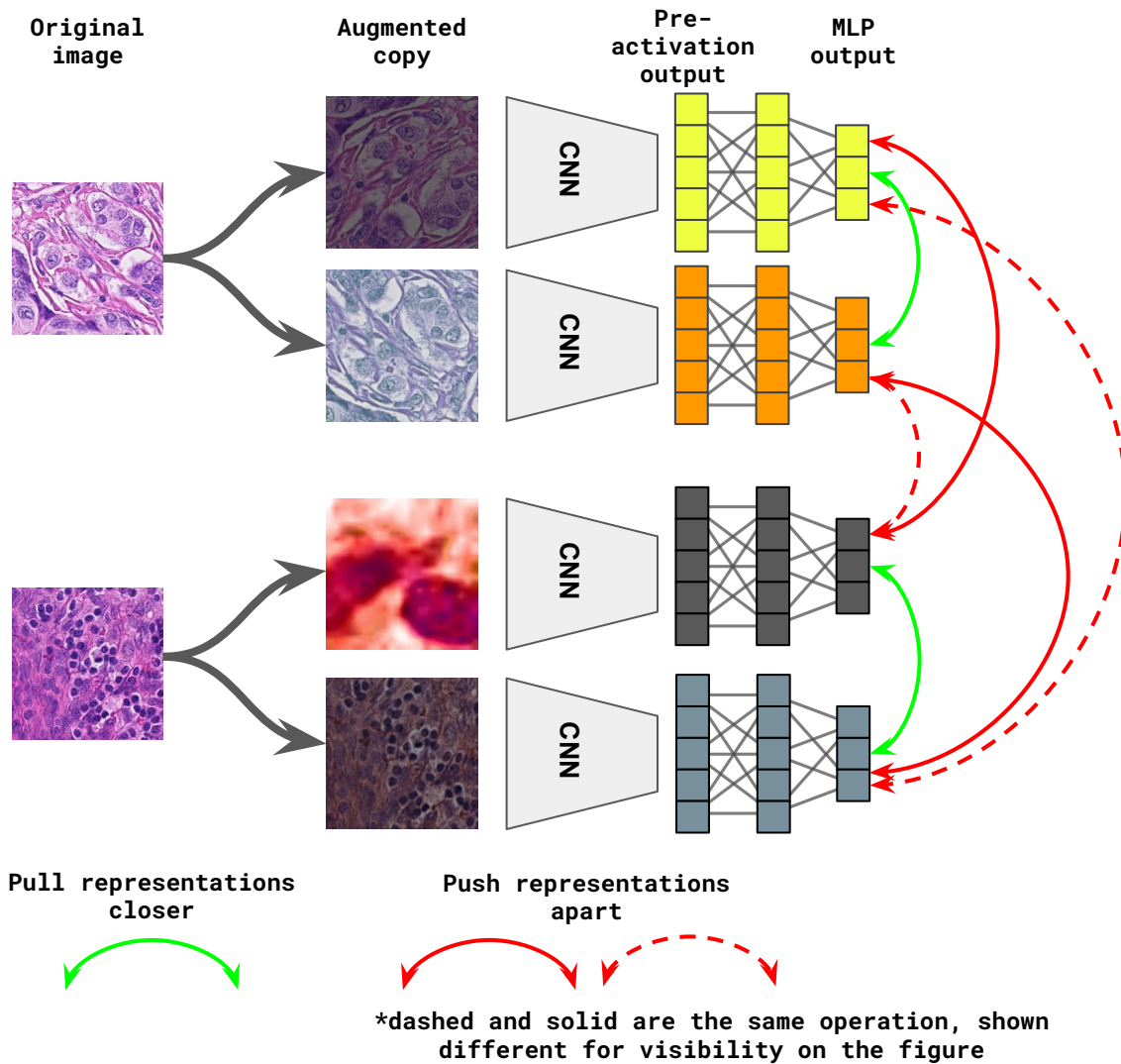


Figure 1: Overview of the method. The block represented as *CNN* is identical for all image patches, and only replicated in the figure for clarity. While the augmented image patches from the same original source are pulled together (green arrows) in the feature space, image patches from different sources are pushed apart (both solid and dashed red arrows represent an identical push operation, shown as such in figure for clarity). The figure is inspired from Chen et al. (2020a).

cases, labeling must also be done on-site due to regulations regarding dissemination of private patient data. In any medical image analysis task, the most laborious and time-consuming step tends to be labeling the data and several approaches have been proposed to mitigate this *data annotation bottleneck*. Unsupervised and self-supervised methods that can utilize unlabeled data, and semi-supervised methods that use partially labeled data, have been found to significantly improve task performance Peikari et al. (2018); Komura and Ishikawa (2018); Campanella et al. (2019).

A common reason for overfitting to neural networks, especially in low data regimes, is feature memorization. Without any prior knowledge, the network quickly learns features that help to decrease the training loss but are not generalizable to an unseen test set. Pretraining aims to learn more general features which can be fine tuned for better performance. While most practitioners use ImageNet pretraining to mitigate overfitting, these features are learned on natural-scene images. Due to differences between such images and the histopathology domain, a certain fraction of these pretrained features are unlikely to be useful for histopathology tasks. This leads to capacity underuse, and creates a generalizability gap. To mitigate these issues, self-supervised learning aims to learn features from raw data from the domain of interest without using any labels.

Until recently, most self-supervised techniques have relied on natural-scene image properties which are not applicable to histopathology images. However, recent contrastive learning approaches can be applied to digital pathology images (see Section 2). In this work, we use residual networks pretrained with self-supervised learning to learn generalizable features. We employ SimCLR Chen et al. (2020a), a contrastive self-supervised technique that has comparable performance to the supervised ResNet 50 network. We train and evaluate the performance of this method on multiple tasks on multiple, multi-organ digital histopathology datasets and aim to find answers to the following questions: What type of data leads to a good representation? Is it possible to use histopathology images to pretrain networks that are better initializations for downstream tasks than networks pretrained on common natural-scene datasets such as ImageNet? Can images from one tissue type help to learn representations for a different tissue type? Can cross-domain learning improve the representations beyond a single tissue type or modality by incorporating information that may not be readily available in a single domain? How important are certain properties such as staining and resolution in learning generalizable features? What is the minimum number of image patches necessary for learning representations? Is it more important to have diversity in the dataset pool, or is it more important to exhaustively train on datasets using all available image patches?

2. Related work

Unsupervised learning has been a long-standing goal of computer-aided diagnostic systems. Previously, sparse and variational autoencoders have been used for unsupervised nuclei detection and transfer learning (e.g., learning filter banks at multiple scales) Xu et al. (2015); Chang et al. (2017); Hou et al. (2019) and generative adversarial networks have been used for tissue and cell-level classification, nuclei segmentation, and cell counting Hu et al. (2018). Most of these unsupervised methods are not applicable to structures larger than cells or to tasks more complicated than distinguishing tissue and cell types. They may also require custom networks, and may only be applicable to applications with specific resolution and staining properties.

Self-supervised learning is a promising subclass of unsupervised learning, where the raw input data is used to generate the learning signal instead of a data-independent prior such as mutual information or cluster density. These methods can generally be applied to larger images and work with standard architectures such as residual networks He et al. (2016). Context-based self-supervised methods rearrange the image input and task the network to perform spatial reordering. For instance, Noroozi and Favaro (2016) tile an image into nine square pieces and then shuffle the tiles, whereas Gidaris et al. (2018) rotate the input image in 90° angles. In either case, the aim is to obtain the original input using a neural network, which is effectively pretrained for downstream tasks by performing predictions on tile orderings or rotation angles, respectively. While contextual information can be exploited in natural scene images to obtain meaningful representations, structures within histopathological images are elastic and may form infinitely many valid groupings. Therefore, these techniques are not directly applicable to the histology domain. For instance, predicting rotations is not a viable task for whole slide images, since cells and surrounding structures will have a valid arrangement in the rotated image as well. To our knowledge, the only work specifically designed for histopathological images uses the spatial adjacency as a signal for similarity, and the training task is to label image pairs as similar or dissimilar based on the spatial distance on a whole slide image Goldenblat and Klaiman (2019).

In addition to having only limited applicability for digital histopathology, context-based approaches are based on handcrafted pretext tasks, which may bias and limit the learning. More recently, contrastive approaches based on learning latent-space features by discriminating between unlabeled training samples achieved state-of-the-art results in computer vision tasks without relying on a heuristically modelled pretext task. Such contrastive learning methods assume that under minor transformations, two views of the same image patch should have similar feature representations Becker and Hinton (1992). Importantly, since con-

trastive methods only rely on consistency at the instance level, they do not require any spatial regularity between or within instances and are applicable to digital histopathology images. The consistency assumption has been exploited by Dosovitskiy et al. (2014) to obtain a parametric feature representation for each training instance. Later, Wu et al. (2018) extended Dosovitskiy et al. (2014) into a non-parametric feature representation using a dynamic memory bank to store latent features of data samples. The memory bank is used for selecting negative examples for each training instance, where any image that is not another view or augmentation of the original training instance is considered negative. The memory bank is then used to obtain negative samples without the need to recompute feature vectors. The use of simple image augmentations (e.g., resizing images, horizontal flips, color jittering, etc.) and memory banks have proved successful in learning representations by maximizing the mutual information between latent representations of positives Bachman et al. (2019); Hénaff et al. (2019); He et al. (2020). Data augmentations have also been utilized by applying the appropriate contrastive loss function on the feature vectors of positive and negative image pairs Tian et al. (2019); Misra and Maaten (2020).

Recently, Chen et al. (2020a) proposed a contrastive learning approach that does not require a custom network or a memory bank, but instead relies on using a large number of minibatch instances (≥ 256) for obtaining negative samples per training instance. By doing so, they were able to improve the quality of learned representations by providing more negative samples per training instance over training epochs. Along with a few architectural improvements, this method outperforms aforementioned techniques by a large margin (+7%) and has comparable performance to the supervised ResNet 50 network when its features are used in training a linear classifier for the ImageNet ILSVRC-2012 dataset Russakovsky et al. (2015). This method was later incrementally improved by Grill et al. (2020) through techniques such as exponential moving averaging of the model weights (Tarvainen and Valpola, 2017) or by knowledge distillation and using larger projection layers (Chen et al., 2020b). We choose not to explore these techniques in this paper as the benefits are negligible ($\sim 4\%$ in ImageNet accuracy) compared to the increase in the number of trainable parameters (e.g., ~ 800 million trainable parameters versus ~ 24 million).

3. The method

3.1. Contrastive self-supervised learning

We use the contrastive learning method proposed by Chen et al. (2020a) which relies on maximizing agreement between representations of two stochastically augmented views of the same image (see Fig. 1).

Specifically, given an image i , a probabilistic augmentation function $f_{aug}(\cdot)$, a neural network or an encoder $f_{\theta}(\cdot)$ with parameters θ and an auxiliary projection layer $p_{\hat{\theta}}(\cdot)$ with parameters $\hat{\theta}$, the aim is to match ℓ_2 normalized feature representations of two augmentations of the same image given by $\mathbf{z}_i = p_{\hat{\theta}}(f_{\theta}(f_{aug}(i)))$. Simultaneously, other images in a batch are made dissimilar from the image i through a contrastive loss function called *NT-Xent* (the normalized temperature-scaled cross-entropy loss), defined as

$$\ell_{i,j} = -\log \frac{\exp(\text{similarity}(\mathbf{z}_i, \mathbf{z}_j)/\tau)}{\sum_{k=1}^{2N} \mathbb{1}_{[k \neq i]} \exp(\text{similarity}(\mathbf{z}_i, \mathbf{z}_k)/\tau)}, \quad (1)$$

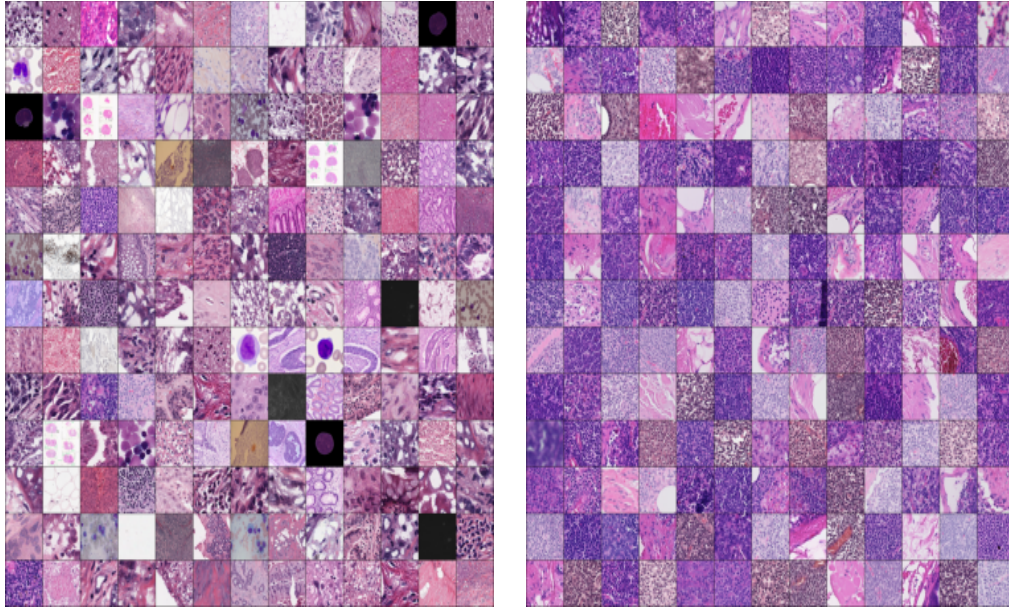
where τ is the temperature parameter that helps weigh different examples to achieve hard negative mining, $\mathbb{1}$ is the indicator function which outputs 1 when $k \neq i$ and 0 otherwise, and the similarity function is a distance metric between two ℓ_2 normalized vectors. For our experiments, we use cosine similarity defined as $\text{similarity}(\mathbf{u}, \mathbf{v}) = \mathbf{u}^T \mathbf{v} / \|\mathbf{u}\| \|\mathbf{v}\|$. The authors experimentally find that NT-Xent helps learn significantly better representations than similar loss functions such as margin Schroff et al. (2015) or logistic Mikolov et al. (2013) losses.

For each training step with a batch size of $2N$, each augmented image has one similar (or positive) and $2(N - 1)$ dissimilar (or negative) samples. By using samples in the same batch as negatives, we avoid the expensive explicit negative example mining and are able to scale up batch sizes where each training step simultaneously optimizes for $\sim 4N^2$ feature vectors.

Defining image diversity for histopathology. The contrastive method exploits the variability in visual properties between image patches to learn salient features. Obtaining visually diverse patches is challenging for digital histopathology, especially when images are viewed under high resolution. Given multiple unlabeled datasets, we assume that selecting images with different staining, resolution and tissue types will lead to a more diverse dataset compared to selecting image patches extracted from the same WSI or sampling images from the same dataset. In our early experiments, we found that pretraining with the dataset constructed using the former approach resulted in better validation performance. Furthermore, when images are inspected visually, the former approach exhibits more diversity (see Fig. 2).

4. Experiments

Unless otherwise stated, all experiments are conducted with the Resnet18 model and fine-tuning training. A dataset with half a million images of size 224×224 pixels can be trained for 1000 epochs using PyTorch on 4 Tesla P100 GPUs in about 24 hours for a Resnet 18 model.



(a) Multiple dataset sampling.

(b) Sampling a single dataset (Camelyon 17).

Figure 2: Defining image diversity in the context of digital histopathology. Images evenly sampled from all 60 datasets visually look more diverse compared to sampling only from a single dataset containing multiple WSIs.

4.1. Hyperparameter and suitable augmentation selection

Setup. We conduct experiments to determine the hyperparameters that will be used in the rest of the paper. We train a Resnet 18 with the method outlined in Section 3.1 with all 60 unlabeled datasets (see Appendix Appendix B.1), where we used a maximum of 1000 image patches per dataset (a total of 48 thousand images). We use the average macro F1 metric on five validation datasets for the classification task to select each hyperparameter. We compare temperatures $\{0.05, 0.1, 0.5, 1, 2, 10\}$ and batch sizes $\{128, 256, 512\}$. We compare Adam Kingma and Ba (2014), Lars You et al. (2017), and Lamb You et al. (2019) optimizers to account for the large batch size. We use learning rates $0.3 \times \text{batchsize}/256$, $\frac{4}{2^{(3 - (\log_2(\text{batchsize}) - 9)/2)} \times 100}$, and 10^{-4} for Lars, Lamb, and Adam, respectively (as proposed by (Chen et al., 2020a) for Lars and by You et al. (2017) for Lamb). We use 10^{-6} as the weight decay.

Since the original set of augmentations were applied on natural-scene images, they may not be suitable for histopathology. We conduct ablation studies on data augmentations with minor modifications. For instance, the original paper uses 8% to 100% randomly resized crops, whereas we compare minima $\{1\%, 5\%, 25\%\}$, with 100% as the maximum in all settings. We train for 1000 epochs per experiment. Since loss is a function of the temperature, performance cannot be assessed by comparing different values of the loss. Therefore each pretrained network is assessed on independent validation datasets.

Data augmentations. In our experiments, we employ randomly resized crops, 90° rotations, horizontal and vertical flips, photometric manipulation (color jittering) and Gaussian blurring as augmentations. We randomly select a rectangle corresponding to 15 to 100% of the area of the original image patch and resize it to the original image’s size, stochastically rotate images with degrees $\in \{0^\circ, 90^\circ, 180^\circ, 270^\circ\}$ with equal (25%) probability, flip in each axis with 50% probability, and compare color jittering strategies where we adjust (brightness, contrast, saturation, hue) of a given image by a percentage value of the original image. Specifically, we compare three types of jittering augmentations with different strengths: light (brightness=0.4, contrast=0.4, saturation=0.4, hue=0.2), medium (0.8, 0.8, 0.8, 0.2) and heavy (0.8, 0.8, 0.8, 0.4). Each number in parentheses represents the fraction of possible change in the corresponding color property, e.g., $\pm 40\%$ shift in brightness in the light jittering augmentation setting. A 100% change in brightness can mean a fully dark image (0% brightness) or doubling the brightness value (200%). Finally, we employ Gaussian blurring 50% of the time, with standard deviation $\sigma \sim \mathcal{U}[0.1, 2.0]$ and kernel size $0.1 \times$ image patch’s side length.

Setting	BACH		Patch Camelyon		BreakHis		NCT-CRC-HE-100K		PANDA		Average	
	Acc.	F_1	Acc.	F_1	Acc.	F_1	Acc.	F_1	Acc.	F_1	Acc.	F_1
Lamb ($\tau = 0.5$)	77.0	76.4	88.4	88.3	81.6	79.0	99.2	99.2	79.5	65.1	85.1	81.6
Lamb ($\tau = 0.1$)	78.0	77.8	88.6	88.5	83.3	80.9	99.1	99.1	79.8	64.8	85.8	82.2
Lamb ($\tau = 0.5$)	70.0	68.8	88.6	88.5	81.2	78.0	99.2	99.2	79.7	65.6	83.7	80.0
Lars ($\tau = 0.05$)	84.0	83.3	89.6	89.5	80.8	77.8	99.0	99.0	79.6	63.5	86.6	82.6
Lars ($\tau = 0.1$)	84.0	83.7	88.7	88.7	82.6	80.2	99.4	99.4	79.9	65.6	86.9	83.5
Lars ($\tau = 0.5$)	79.0	78.7	89.3	89.2	82.2	78.8	99.2	99.2	80.3	65.7	86.0	82.3

Table 1: Selection of optimizer and temperature hyperparameters.

Results. In our initial experiments, we observed Adam did not converge for batch sizes ≥ 256 and was discarded. We observed Lars outperformed Lamb in most settings, and was therefore used for the remaining experiments. Interestingly, we found that randomly cropping 1% of the image patch and resizing to its original size outperformed both 5% and 25%, by over 1% in macro F1 score and over 0.5% in accuracy. We found color jittering strongly correlated with the quality of learned representations. No color jittering has the lowest training loss since it is easy to distinguish images without tampering their color properties, however, it was outperformed by both light (+6.7% in F1) and strong (+7.7% in F1) jittering settings. Overall, we observed that more aggressive augmentations resulted in better representations. For instance, while 1% of a 224×224 patch (a 2×2 square) cannot be used to distinguish the original patch it was extracted from, it still outperformed {5%, 25%}. We argue that the improvement is due to a regularization effect on the contrastive objective, which prevents saturation and enables the learning of more salient features. We found that smaller temperatures generally perform better, and larger ones (1, 2, 10) tend not to converge, or have very poor validation performance. However, we found that while 0.05 performed better than 0.5 (1.6% in F1 for Lamb and 0.3% for Lars), 0.1 performed best, beating 0.05 (0.6% in F1 for Lamb and 0.9% for Lars). For the full list of experiments, please refer to tables 1 and 2.

4.2. Validation experiments

Tasks. We validate pretrained networks trained under multiple settings (e.g., training only with a single dataset or tissue type, different number of training images etc.) on 5 classification, 3 segmentation and 1 regression datasets. See Appendix Appendix B.2 for the detailed explanation of each validation set. We compare pretrained networks with randomly initialized and ImageNet pretrained Resnet 18, 34, 50 and 101. We compare two training settings: fine-tuning and last layer training. In order to assess the learned representations directly, we freeze each residual network at the pre-activation layer and only train a linear classifier or

Setting	BACH		Patch Camelyon		BreakHis		NCT-CRC-HE-100K		PANDA		Average	
	Acc.	F_1	Acc.	F_1	Acc.	F_1	Acc.	F_1	Acc.	F_1	Acc.	F_1
Baseline	78.0	77.8	88.6	88.5	83.3	80.9	99.1	99.1	79.8	64.8	85.8	82.2
No jitter	55.0	54.6	87.0	86.9	79.5	75.2	98.1	98.1	79.2	59.4	79.8	74.8
Medium jitter	76.0	74.7	89.0	88.9	81.5	78.7	99.3	99.3	80.5	65.8	85.3	81.5
Heavy jitter	84.0	83.5	89.0	88.9	80.7	78.2	98.9	98.9	79.8	63.2	86.5	82.5
Random crop (1%)	83.0	82.4	88.9	88.8	83.5	81.0	99.2	99.2	80.1	67.7	86.9	83.8
Random crop (5%)	77.0	77.0	89.1	89.0	83.2	80.3	99.4	99.4	80.1	65.4	85.7	82.2
Random crop (25%)	82.0	81.8	89.2	89.1	81.7	79.0	99.1	99.1	79.9	63.5	86.4	82.5

Table 2: Selecting suitable augmentations for self-supervised learning on digital histopathology tasks. Baseline augmentations consist of $\in \{0^\circ, 90^\circ, 180^\circ, 270^\circ\}$ image rotations, flips in each axis with 50% probability, Gaussian blurring, and light color jittering.

a regressor on the learned representations (*last layer* training). This setting is omitted for the segmentation task, since the UNet-like decoder (Yakubovskiy, 2020) that we use contains a comparable number of trainable parameters to the pretrained Resnet encoder, and can encode information beyond encoder features. We also train each network without freezing any layers (*fine-tuning*). While fine-tuning is commonly employed, freezing various layers of a network may be used to avoid overfitting whenever the training dataset is small. Furthermore, pretrained features can also be used in clustering (see Section 4.4), feature selection, and in more traditional machine learning methods such as decision trees and support vector machines.

Setup. We train for 100 epochs per experiment, use Adam optimizer, a batch size of 32 with a weight decay of 0.00001 for Resnet18 models, and 0.0001 otherwise. We use 50% of the original dataset as the training, 25% as validation, and 25% as the test set. We use accuracy and macro F1 score as our validation metrics for the classification task. Accuracy is an indicator of the overall performance whereas macro F1 weighs each class equally regardless of the number of samples per class, which accounts for the class imbalance seen in most digital histopathology datasets. For tables regarding classification experiments, Acc. stands for overall accuracy and F_1 is the macro F_1 score. For the segmentation task, we compute macro and micro F1 scores, where the former is equivalent to the Dice score for binary segmentation tasks (e.g., foreground vs. background) and the latter is equivalent to accuracy. For the regression task, we compute mean squared error (MSE) and the mean absolute error (L_1) on the predictions and the ground truth regression labels (varying between 0 to 100%). The test metrics corresponding to the maximum validation metrics are reported.

4.3. Pretraining is most useful when only a small number of training images is available

It is generally accepted that pretrained networks boost the performance in medical image analysis (Tajbakhsh et al., 2016) and digital histopathology tasks (Mehra et al., 2018). We conduct validation experiments on the

classification task for all datasets using {1, 2, 5, 10, 20, 50, 75, 100}% of each training dataset. By limiting the amount of training data, we compare the effect of training dataset size on different pretraining settings. Specifically, we compare random initialization, ImageNet pretraining and self-supervised pretraining for networks Resnet 18, 34, 50 and 101. We report average of results on figures 6, C.10, C.13, and C.16 and detailed results per dataset on figures 7, C.11, C.14, and C.17.

We found that in the absence of a large training set, training a classifier using a pretrained initialization can significantly improve the performance (up to double the accuracy on *BACH* dataset with only one sample per class, see Fig. 7), whereas these effects are diminished on a larger dataset (e.g., Patch Camelyon where the accuracies of random initialization and self-supervised initialization are equal when 20% of the training set is used). Furthermore, the bias introduced by pretraining can lead to suboptimal convergence by limiting the exploration of hypothesis space, whereas a random initialization can achieve better performance if enough samples are provided (e.g., *Patch Camelyon* with 131 thousand samples can outperform both ImageNet and self-supervised initializations, see Fig. 7).

Interestingly, we found that ImageNet performed slightly better for the Resnet 34 model, and obtained the highest macro F_1 score. In contrast, the best performance in terms of accuracy was achieved with Resnet 18 using self supervision. This is unlike some recent work that shows for various histopathology tasks, models comparable to Resnet 34 in terms of network capacity tend to perform significantly better than both smaller and larger models (Campanella et al., 2019). As Resnet 34 has more than double the parameters of Resnet 18, self supervision can be used for obtaining better results using a smaller model.

4.4. Features obtained by pretraining are more representative for histopathological image patches than ImageNet features

We compare representations learned through self-supervision with the pretrained ImageNet features by training linear classifiers on the pre-activation layer of the Resnet models. For Resnet 18 and Resnet 34, this amounts to 512 features, and to 2048 features for Resnet 50 and Resnet 101. The self-supervised network achieves significantly better results despite updating the batch statistics for the ImageNet network to match the training data (figures 6c, 6d). This indicates our method has learned domain-specific features which can be useful especially when training samples are scarce. One may freeze and obtain features from various layers of the network for training various machine learning models including neural networks, support vector machines or random forest classifiers. We performed the same comparison for the regression task, where we froze the network at the pre-activation layer and trained a single regression layer and obtained a similar

outcome. For segmentation tasks, we use a UNet architecture (Ronneberger et al., 2015) which contains a pretrained encoder and a randomly initialized decoder. Since a decoder can contain millions of parameters which can be trained to achieve satisfactory performance regardless of the encoder weights, we do not include analogous frozen encoder experiments for the segmentation task.

When models are fine tuned without freezing any layers, self-supervision still outperforms the ImageNet (figures 6a, 6b); however, the gap in performance between two initializations are significantly reduced. Furthermore, we find that as the network capacity (i.e., the model size) increases, the gap between last layer training for two initializations also decrease.

Unsupervised clustering using the learned representations. Learned representations can be directly used for clustering without any labeled training examples. In this section, we use learned representations to cluster image patches extracted from WSIs. Note that the learned features can also be used for querying an image to its nearest neighbors without clustering the dataset, which is useful in applications such as active learning for sample selection and various data retrieval systems.

Negative mining is an important task in most tasks involving WSIs. For illustration of the saliency of learned representations, we perform negative mining on WSIs from a dataset including post-neoadjuvant therapy BRCA specimens with annotations of regions containing tumor (Peikari et al., 2017; Martel et al., 2019). Randomly sampling patches from a WSI will result in a large class imbalance in favor of negatives, which leads to an increased ratio of false negatives. One may mitigate this issue by aggregating the sampled patches and selecting a subset of “representative” patches. This is done by clustering, where we rely on the perceived visual or morphological similarity of patches according to their relative distance to each other in the feature space. Specifically, we sample 1.4 million images from 69 WSIs and cluster images using their feature representations generated by the Resnet18 trained using self supervision. The features are clustered using the mini-batch K-means algorithm. The resulting clusters can be seen in Fig. 3 with three samples per cluster. In addition, we select a few clusters and highlight them on WSIs to segment various regions of interests without any supervision on figures 4, and 5.

4.5. Having a small diverse set of images is better than a having large number of images that look similar

Some of the datasets that we are using for training are comprised of WSIs. Each WSI is very large and it is not feasible to sample the whole image. For instance, TUPAC 2016 Veta et al. (2019) contains 500 WSIs and only extracting patches of size 224×224 pixels at $0.25\mu\text{m}/\text{pixel}$ that contain foreground (refer

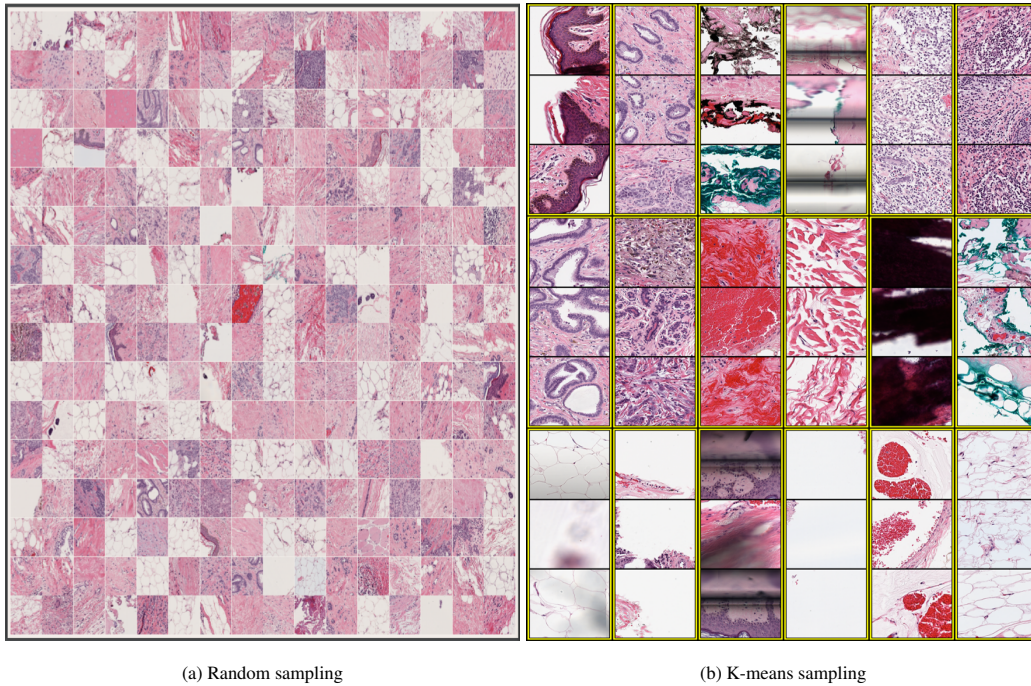


Figure 3: Sampling image patches from whole-slide images randomly versus feature based K-means clustering. Each figure is extracted from an actual experiment. In Fig. 3b, each yellow box shows three samples closest to the center of a randomly selected cluster for illustration. Note that visually similar patches with features such as out-of-focus regions, creases, ink marks of *different colors*, morphological structures such as ducts, outlines of the nipple, and red blood cells are clustered together. Furthermore, patches with varying nuclei formation patterns are also clustered roughly according to their density.

Setting	BACH		Patch Camelyon		BreakHis		NCT-CRC-HE-100K		PANDA		Average	
	Acc.	F_1	Acc.	F_1	Acc.	F_1	Acc.	F_1	Acc.	F_1	Acc.	F_1
10 samples/dataset	74.5	74.4	87.4	87.3	82.5	76.4	92.2	89.2	76.6	54.0	82.6	76.3
0.1%	79.0	79.1	87.2	87.1	81.9	75.2	94.4	92.6	76.4	57.2	83.8	78.2
1%	81.5	81.3	86.7	86.6	81.2	72.6	92.9	91.4	79.1	58.8	84.3	78.1
10%	75.5	75.0	84.4	84.1	81.9	73.3	93.8	92.4	75.4	57.6	82.2	76.5
10% (<i>early stop, 200 epochs</i>)	77.0	76.2	85.4	85.2	81.4	73.8	92.7	90.1	74.8	62.0	82.3	77.5

Table 3: Classification experiments for dataset size. 0.1% corresponds to ~ 4 thousand images. 10 samples per dataset setting contains ~ 600 images in total.

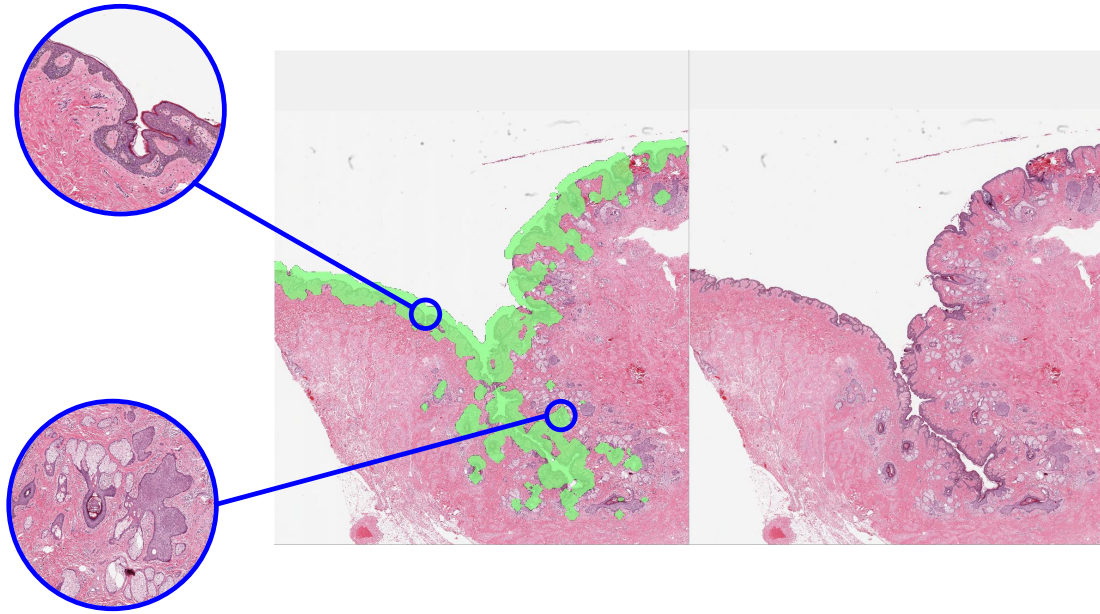


Figure 4: Squamous regions are highlighted.

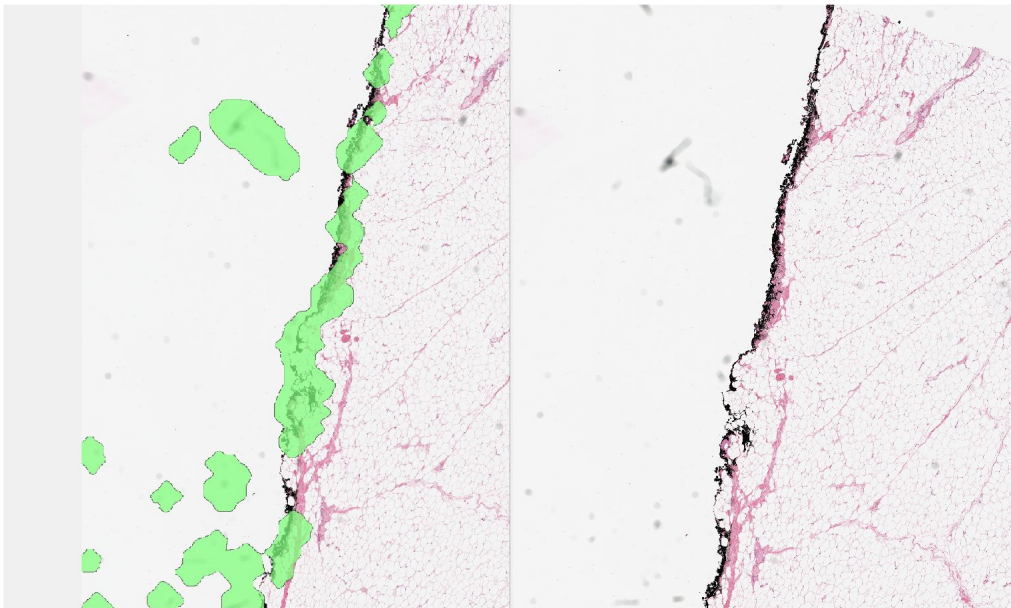


Figure 5: Clusters representing creases, out of focus regions, and smears are highlighted.

Setting	BACH		DigestPath2019		Gleason2019		Average	
	Micro F_1	Macro F_1	Micro F_1	Macro F_1	Micro F_1	Macro F_1	Micro F_1	Macro F_1
10 samples/dataset	78.9	40.9	86.1	67.8	55.1	33.0	73.4	47.2
0.1% of data	80.2	40.6	86.8	71.9	53.5	32.2	73.5	48.2
1% of data	78.8	39.5	87.5	73.9	56.2	35.6	74.2	49.7
10% of data	82.2	42.1	87.6	73.6	48.1	29.0	72.6	48.2
10% (<i>early stop, 200 epochs</i>)	78.6	39.4	87.2	72.3	54.3	34.0	73.4	48.6

Table 4: Segmentation experiments for dataset size. 0.1% corresponds to ~ 4 thousand images. 10 samples per dataset setting contains ~ 600 images in total.

Setting	BreastPathQ	
	L_1	MSE
10 samples/dataset	0.102	0.019
0.1%	0.08	0.01
1%	0.10	0.01
10%	0.55	0.49
10% (<i>early stop, 200 epochs</i>)	0.17	0.05

Table 5: Regression experiments for dataset size. 0.1% corresponds to ~ 4 thousand images. 10 samples per dataset setting contains ~ 600 images in total.

to Appendix Appendix A), we obtain more than five million patches. Furthermore, many of the TCGA-* datasets each contain more than 1000 WSIs, therefore using all images quickly becomes intractable.

Instead, we randomly sample a maximum of 100 patches from each WSI and use all images from non-WSI datasets to generate the unsupervised training data. We use the maximum available resolution per WSI, which is $\sim 0.25\mu\text{m}/\text{pixel}$ or $\sim 0.50\mu\text{m}/\text{pixel}$ depending on the dataset. We use 206 thousand images from 26 non-WSI datasets, and sample over four million patches from 35 WSI datasets containing around 25 thousand WSIs. We compare using $\{0.1, 1, 10\}\%$ of the sampled datasets with a maximum of two thousand and a minimum of 10 images per dataset if the number of images corresponding to the percentage setting for a dataset is below 10. In the end, we obtain 4, 40 and 400 thousand images per percentage setting. In addition, we pretrain a model using only 10 images per dataset (~ 600 training images in total). In this setting, we sample 10 image patches from each WSI dataset as well, which can contain a few *million* image patches across all WSIs in that dataset. Therefore, the dataset is drastically undersampled. We do not conduct experiments with 100% of sampled images since we observed deteriorated performance with 10% setting compared to 1%. We report results on tables 3, 4, 5.

We found that using a smaller training set outperforms using a training set with more images. Specifi-

cally, we found that using 0.1% vs. 1% was comparable among different tasks. Using 10% of the images was outperformed by all settings by a large margin for regression and segmentation tasks, and was on par with the 10 samples per dataset setting on classification tasks.

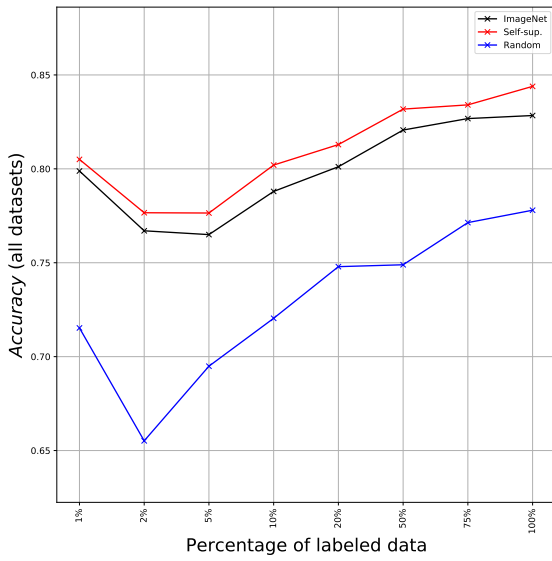
The degradation in performance when a large number of images are used is likely due to oversampling; if one region of tissue is oversampled resulting in a large number of very similar appearing patches, then the network may rely on features that are not generalizable in order to separate them. To reduce noisy encoding, we trained the network for only 200 epochs (as opposed to 1000), and observed slightly better results. However, these results are still not comparable to 1% setting. Hence, we find that for histopathological images, a moderately sized training set with a diverse set of images is crucial for obtaining useful representations.

4.6. Transferability of features between tissue types, staining, and resolutions

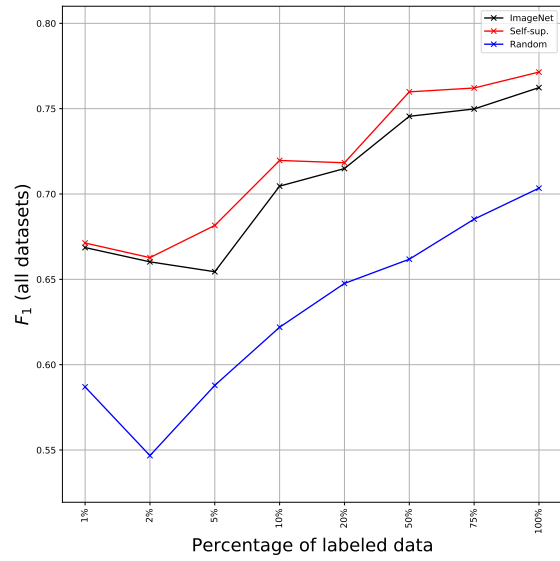
To assess if it is better to pretrain using datasets drawn exclusively from a similar tissue type to that present in the target task, we conducted separate experiments using Resnet 18 with three different tissue types: breast, lymph nodes and prostate. Specifically, we trained a network using only Camelyon 16 and Camelyon 17 datasets for lymph nodes, and TCGA-PRAD and Prostate-MRI datasets for prostate. Due to the greater availability of data for breast, we trained on a larger number of datasets: TCGA-BRCA, BACH challenge dataset, TUPAC16, BreakHis, TNBC, several datasets from Andrew Janowczyk, BreastPathQ, ICPR2014 and ICPR2012 (see Table B.13). For each experiment, roughly the same number of training images were used (~ 40 thousand).

Despite the site-specific training (i.e., the tissue used in pretraining), we did not observe significant correlation between the trained model and the validation performance. For instance, lymph models significantly outperformed breast models on the BACH dataset for breast cancer classification. Similarly, the prostate model was outperformed by the breast model on the prostate cancer grading task on the Gleason 2019 dataset. In addition, we observed poorer performance compared to training with all datasets (tables 9, 11, 12). For a full list of results, please refer to tables 6, 7, and 8.

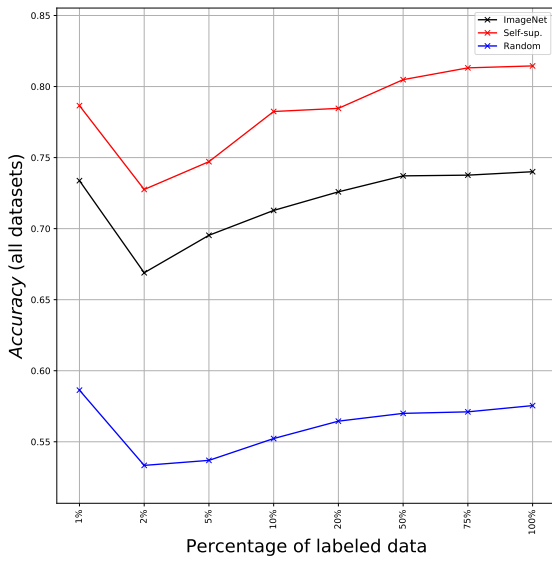
We believe the lack of correlation, and the degradation compared to using all tissue types can be due to the following factors: (1) limitations of the contrastive approach where representations are incapable of encoding domain specific information in the absence of the *other tissue types*, (2) convolutional networks are highly sensitive to visual properties such as staining, resolution and morphological shapes, and do not encode abstract features in the absence of a specific objective (e.g., cancer grading), (3) the network can only be *incentivized* to encode a richer representation given a diverse training dataset.



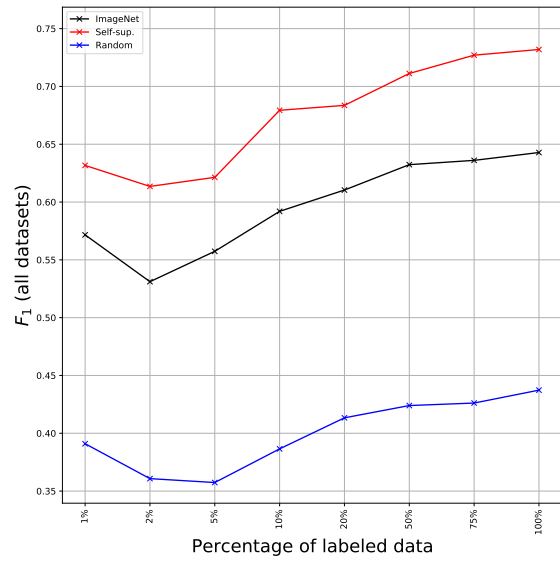
(a) Accuracy (fine tuning)



(b) Macro F_1 (fine tuning)



(c) Accuracy (last layer)



(d) Macro F_1 (last layer)

Figure 6: Average classification performance for both fine tuning and last layer settings on five datasets for the pretrained Resnet 18 model.

Tissue	BACH		Patch Camelyon		BreakHis		NCT-CRC-HE-100K		PANDA		Average	
	Acc.	F_1	Acc.	F_1	Acc.	F_1	Acc.	F_1	Acc.	F_1	Acc.	F_1
Breast	78.0	77.6	85.8	85.6	83.5	76.8	94.1	92.2	77.5	61.3	83.8	78.7
Prostate	80.0	79.7	85.8	85.6	84.1	77.0	93.6	91.5	78.4	57.7	84.4	78.3
Lymph	78.5	78.3	87.4	87.3	81.0	73.7	94.2	92.1	77.8	64.8	83.8	79.2

Table 6: Classification experiments for feature transferability intra/inter organs.

Tissue	BACH		DigestPath2019		Gleason2019		Average	
	Micro F_1	Macro F_1	Micro F_1	Macro F_1	Micro F_1	Macro F_1	Micro F_1	Macro F_1
Breast	74.6	35.7	86.2	72.6	59.2	35.8	73.3	48.0
Prostate	79.9	40.4	87.3	72.6	56.6	34.2	74.6	49.1
Lymph	84.3	43.5	85.7	72.6	52.9	28.7	74.3	48.3

Table 7: Segmentation experiments for feature transferability intra/inter organs.

Organ	BreastPathQ	
	L_1	MSE
Breast	0.132	0.028
Prostate	0.121	0.025
Lymph	0.13	0.03

Table 8: Regression experiments for feature transferability intra/inter organs.

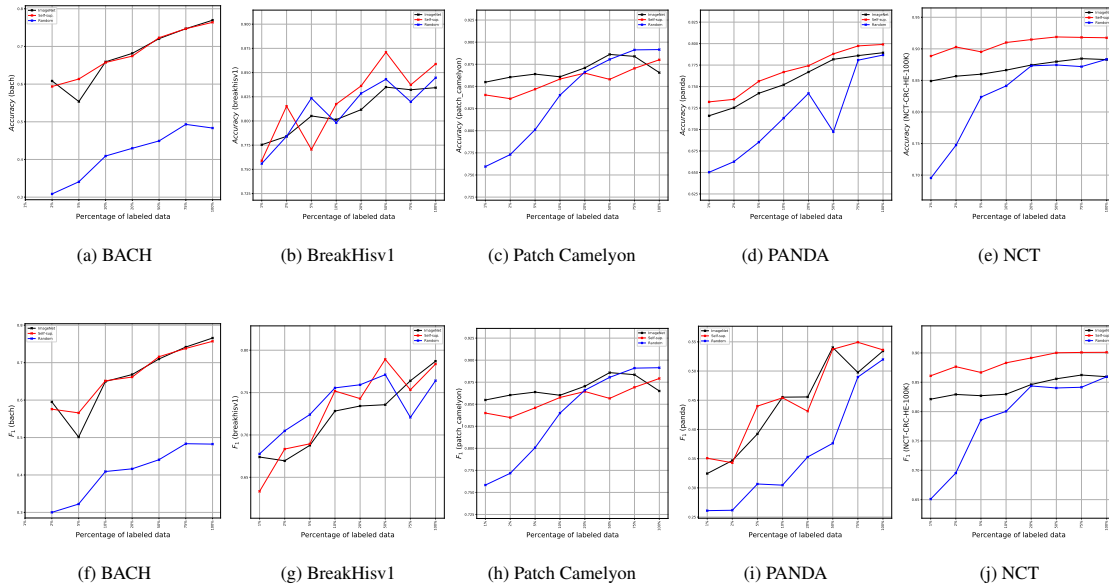


Figure 7: Classification performance for fine tuning setting on five datasets for the pretrained Resnet 18 model.

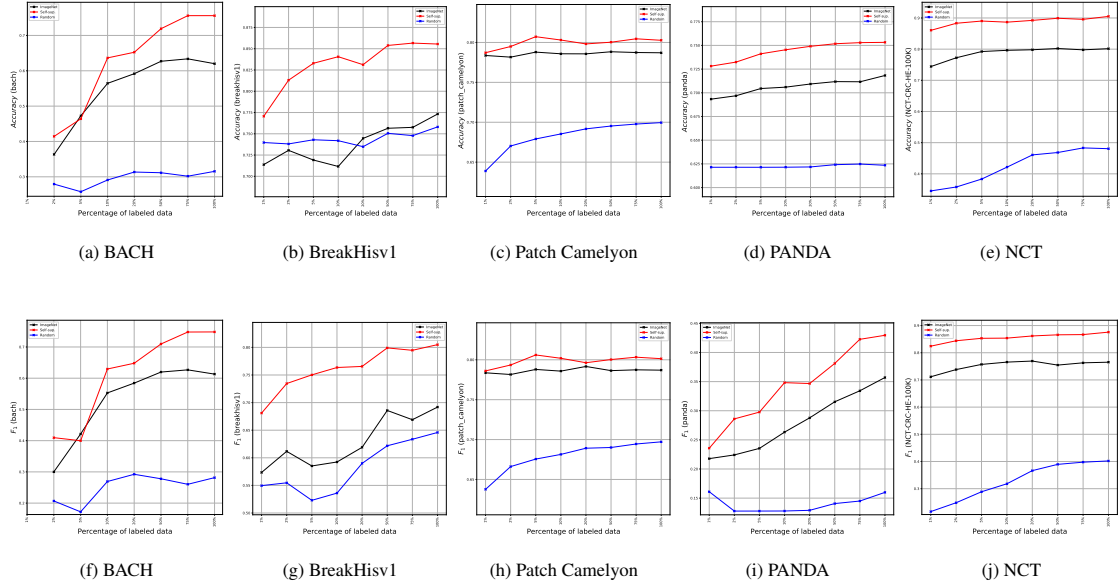


Figure 8: Classification performance for last layer setting on five datasets for the pretrained Resnet 18 model.

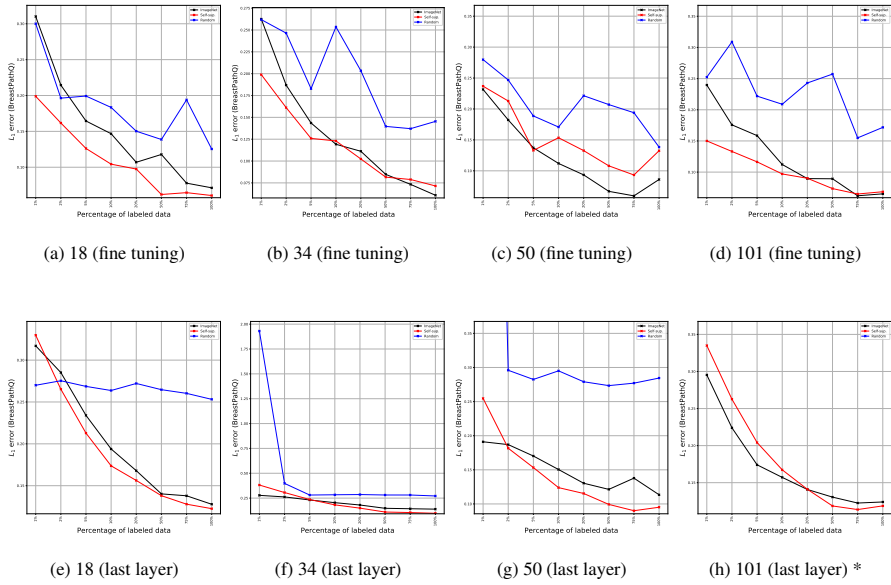


Figure 9: * Randomly initialized network's error is too large to fit in the plot. Regression results showing the mean absolute error (L_1) on the BreastPathQ dataset for four differently sized Resnet models with fine tuning and linear regression on the frozen features. Unlike classification and segmentation, differences between ImageNet and self-supervised pretraining are less emphasized.

Resnet-	Pretraining	BACH		Patch Camelyon		BreakHis		NCT-CRC-HE-100K		PANDA		Average	
		Acc.	F_1	Acc.	F_1	Acc.	F_1	Acc.	F_1	Acc.	F_1	Acc.	F_1
18	Random	48.3	48.2	89.2	89.1	84.5	76.4	88.3	85.9	78.7	52	77.8	70.3
	ImageNet	77	76.6	86.6	86.5	83.4	78.7	88.3	86	78.9	53.4	82.8	76.2
	Ours	76.4	75.7	88	87.9	85.9	78.4	91.8	90.1	79.9	53.6	84.4	77.1
34	Random	45	44.9	89.1	89	83.7	74.4	91.5	88.7	77.2	51.4	77.3	69.7
	ImageNet	78.5	78	87.6	87.5	82.5	73.8	93.5	91.3	75.6	57.3	83.6	77.6
	Ours	71.4	70.4	88.7	88.5	82.6	75.1	93.8	91.5	77.2	51.1	82.8	75.3
50	Random	46	43.8	87.3	87.2	84.6	78.5	91.4	88.8	78.8	50.4	77.6	69.7
	ImageNet	75	73.9	83.6	83.2	81.4	74	93.9	91.7	75.6	53.6	81.9	75.3
	Ours	76.5	76.1	89.2	89.1	79	73.4	92.9	89.7	77.6	50.4	83.1	75.7
101	Random	47.5	46.7	85.5	85.3	80.5	71.1	93	90.6	79.5	54.6	77.2	69.7
	ImageNet	76	74.6	83.6	83.3	84.7	78.3	93.5	91.4	75.5	55.2	82.7	76.6
	Ours	72.4	71.2	88.3	88.1	84.3	76.5	94.6	91.7	75.8	48.1	83.1	75.1

Table 9: Classification experiments for four differently sized Resnet models with fine tuning. We compare random initialization, ImageNet pretraining and self-supervised pretraining.

4.7. Overall comparison

We combine our findings from previous sections and present the final results using the best practices in tables 9, 10, 11, and 12. We find that self-supervised training is comparable to ImageNet on classification (tables 9 and 10) and regression tasks (Table 12). In contrast, results for segmentation tasks (Table 11) show that ImageNet outperforms self supervision by a large margin (up to 7% in macro F_1 scores) for larger models, even though a self-supervised Resnet 18 model achieves comparable performance to the best performing models across all network sizes. This is an important finding, as most papers related to self-supervised learning do not include segmentation tasks in their benchmarks.

5. Discussion and conclusion

Our main objective in this work was to show that, by pretraining, we can learn better features to improve performances on multiple downstream tasks, including classification, regression, and segmentation. The self-supervised method outlined in this paper is the first method to consistently have comparable performance to ImageNet pretraining without additional complexity. To our knowledge, there is no prior research on histopathological image analysis with a training regimen that consistently reaches or surpasses supervised training. In addition, this is the first study which uses a very large number of images in digital histopathology

Resnet-	Pretraining	BACH		Patch Camelyon		BreakHis		NCT-CRC-HE-100K		PANDA		Average	
		Acc.	F_1	Acc.	F_1	Acc.	F_1	Acc.	F_1	Acc.	F_1	Acc.	F_1
18	Random	31.5	28.2	70	69.7	75.8	64.6	48.1	40.2	62.4	16	57.5	43.7
	ImageNet	62	61.3	78.7	78.7	77.3	69.2	80.2	76.5	71.8	35.7	74	64.3
	Ours	75.6	74.8	80.3	80.1	85.6	80.5	90.5	87.6	75.3	42.9	81.5	73.2
34	Random	29.5	23.5	66.9	65.3	80.7	71.2	49.1	40	62.3	13.2	57.7	42.6
	ImageNet	63.5	62.8	79.8	79.8	78.1	69	87.7	84	71.8	30.8	76.2	65.3
	Ours	68.8	68.3	80.1	80	78.2	69.7	90.3	86.7	74.5	34.6	78.4	67.9
50	Random	35.5	31.7	71.2	71.1	82.5	73.4	41.4	31.4	58.9	19.5	57.9	45.4
	ImageNet	62.5	61.8	81	81	79.8	71.8	88.9	85.3	73.1	35.6	77.1	67.1
	Ours	65.8	65.4	80.3	80.1	78.9	71.8	91	87.6	75.5	36.6	78.3	68.3
101	Random	25	10	53.8	41.6	60.7	57.2	23.5	12.7	62.1	12.8	45	26.9
	ImageNet	64.5	63.5	80.6	80.5	79	71.1	84	80.6	63.7	25.8	74.4	64.3
	Ours	73.4	72.6	82.6	82.5	76.4	70.1	81.7	78.6	70.5	31.2	76.9	67

Table 10: Classification experiments for four differently sized Resnet models with linear regression on the frozen features (last layer training). We compare random initialization, ImageNet pretraining and self-supervised pretraining.

Resnet-	Pretraining	BACH		DigestPath2019		Gleason2019		Average	
		Micro F_1	Macro F_1	Micro F_1	Macro F_1	Micro F_1	Macro F_1	Micro F_1	Macro F_1
18	Random	79.4	43.2	88.8	78.8	57.6	34.6	75.2	52.2
	ImageNet	77.1	47.3	92.4	84.3	65.2	40.6	78.2	57.4
	Ours	85.3	53.3	90.9	82.3	66.9	42.0	81.0	59.2
34	Random	79.7	46.2	88.5	72.1	53.5	30.9	73.9	49.7
	ImageNet	75.2	54.9	92.3	83.5	66.2	41.6	77.9	60
	Ours	77	44.3	91.1	79.7	61.9	34.8	76.7	53
50	Random	66.4	27.4	88.2	78.2	54	31.5	69.5	45.7
	ImageNet	84.8	59.6	92.9	84.5	64	40.3	80.5	61.4
	Ours	76	39.4	90.6	81.5	63.7	40.6	76.7	53.8
101	Random	71.9	35.6	88.2	73.6	51.2	29.7	70.4	46.3
	ImageNet	85.1	48.3	90.9	81.4	64.7	40.3	80.2	56.6
	Ours	87.6	47	89.5	70.8	61.6	38.5	79.6	52.1

Table 11: Segmentation experiments for four differently sized Resnet models with fine tuning training. We compare random initialization, ImageNet pretraining and self-supervised pretraining.

Resnet-	Pretraining	BreastPathQ (<i>fine-tuning</i>)		BreastPathQ (<i>last layer</i>)	
		L_1	MSE	L_1	MSE
18	Random	0.13	0.03	0.25	0.09
	ImageNet	0.08	0.01	0.12	0.02
	Ours	0.06	0.01	0.12	0.02
34	Random	0.15	0.03	0.25	0.10
	ImageNet	0.07	0.01	0.14	0.03
	Ours	0.07	0.01	0.12	0.03
50	Random	0.14	0.04	0.28	0.12
	ImageNet	0.08	0.01	0.12	0.03
	Ours	0.14	0.01	0.09	0.02
101	Random	0.17	0.04	0.877	0.44
	ImageNet	0.06	0.01	0.13	0.03
	Ours	0.06	0.01	0.13	0.03

Table 12: Regression experiments for four differently sized Resnet models with linear regression on the frozen features (last layer training). We compare random initialization, ImageNet pretraining and self-supervised pretraining.

setting: 26 image datasets with over 206 thousand patches and ~ 25 thousand gigaresolution images in 35 datasets that consist of whole-slide images.

We have shown that the success of the contrastive pretraining method heavily relies on the diversity of the unlabeled training set, as opposed to the number of images. This is an important consideration when one adopts a technique from the computer vision community, where most methods are validated on natural scene images that contain significantly more diversity than medical images. Furthermore, we have shown that the site which the training images were extracted from did not have a significant effect on the quality of learned representations, as shown in Section 4.6. While this shows a clear divergence from the training of human experts who focus on a specific organ, it also can significantly increase the number of available datasets in training such systems.

The method used in this paper was subsequently improved by techniques such as knowledge distillation (Hinton et al., 2015) and using a three layer projection layer with the second layer as the pre-activation layer (Chen et al., 2020b). We did not employ such techniques in this paper as these techniques are either not directly related to contrastive learning, or require significant increase in number of trainable parameters. Instead we focused on the simplest contrastive method which significantly improved the state-of-the-art and experimented under multiple settings outlined in Section 4 to understand the capabilities and limitations of the contrastive training for histopathology images. We believe that so long as the fundamentals of the

sample contrastive training framework remain the same, the insights we obtained will still be valid for future work on self-supervision. Overall, we found that contrasting images which are visually distinguishable helped in learning salient representations. In contrast, images which look similar with small nuances that are important in histopathology (e.g., single cell tumors that only occupy a small portion of a given patch) were not suitable for contrastive learning, and led to noisy representations. As this is rarely the case for the natural-scene images, researchers working on digital histopathology images need to address domain-specific issues to bridge the gap between histopathology and computer vision in self-supervised learning.

Conflict of interest

We have no conflict of interest to declare.

Acknowledgments

This work was funded by Canadian Cancer Society (grant #705772) and NSERC. It was also enabled in part by support provided by Compute Canada (www.computecanada.ca).

References

- Akbar, S., Peikari, M., Salama, S., Panah, A.Y., Nofech-Mozes, S., Martel, A.L., 2019. Automated and manual quantification of tumour cellularity in digital slides for tumour burden assessment. *Scientific Reports* 9, 14099.
- Aresta, G., Araújo, T., Kwok, S., Chennamsetty, S.S., Safwan, M., Alex, V., Marami, B., Prastawa, M., Chan, M., Donovan, M., et al., 2019. Bach: Grand challenge on breast cancer histology images. *Medical image analysis* 56, 122–139.
- Bachman, P., Hjelm, R.D., Buchwalter, W., 2019. Learning representations by maximizing mutual information across views, in: *Advances in Neural Information Processing Systems*, pp. 15509–15519.
- Becker, S., Hinton, G.E., 1992. Self-organizing neural network that discovers surfaces in random-dot stereograms. *Nature* 355, 161–163.
- Bulten, W., Litjens, G., Pinckaers, H., Ström, P., Eklund, M., Kartasalo, K., Demkin, M., Dane, S., 2020. The PANDA challenge: Prostate cANcer graDe Assessment using the Gleason grading system. URL: <https://doi.org/10.5281/zenodo.3715938>, doi:10.5281/zenodo.3715938.

- Campanella, G., Hanna, M., Geneslaw, L., Miraflor, A., Silva, V., Busam, K., Brogi, E., Reuter, V., Klimstra, D., Fuchs, T., 2019. Clinical-grade computational pathology using weakly supervised deep learning on whole slide images. *Nature Medicine* 25, 1. doi:10.1038/s41591-019-0508-1.
- Chang, H., Han, J., Zhong, C., Snijders, A.M., Mao, J.H., 2017. Unsupervised transfer learning via multi-scale convolutional sparse coding for biomedical applications. *IEEE Transactions on Pattern Analysis and Machine Intelligence* 40, 1182–1194.
- Chen, T., Kornblith, S., Norouzi, M., Hinton, G., 2020a. A simple framework for contrastive learning of visual representations. *arXiv preprint arXiv:2002.05709* .
- Chen, T., Kornblith, S., Swersky, K., Norouzi, M., Hinton, G., 2020b. Big self-supervised models are strong semi-supervised learners. *arXiv preprint arXiv:2006.10029* .
- Dosovitskiy, A., Springenberg, J.T., Riedmiller, M., Brox, T., 2014. Discriminative unsupervised feature learning with convolutional neural networks, in: *Advances in neural information processing systems*, pp. 766–774.
- Gidaris, S., Singh, P., Komodakis, N., 2018. Unsupervised representation learning by predicting image rotations. *arXiv preprint arXiv:1803.07728* .
- Gildenblat, J., Klaiman, E., 2019. Self-supervised similarity learning for digital pathology. *arXiv preprint arXiv:1905.08139* .
- Grill, J.B., Strub, F., Altché, F., Tallec, C., Richemond, P.H., Buchatskaya, E., Doersch, C., Pires, B.A., Guo, Z.D., Azar, M.G., et al., 2020. Bootstrap your own latent: A new approach to self-supervised learning. *arXiv preprint arXiv:2006.07733* .
- He, K., Fan, H., Wu, Y., Xie, S., Girshick, R., 2020. Momentum contrast for unsupervised visual representation learning, in: *Proceedings of the IEEE/CVF Conference on Computer Vision and Pattern Recognition*, pp. 9729–9738.
- He, K., Zhang, X., Ren, S., Sun, J., 2016. Deep residual learning for image recognition, in: *2016 IEEE Conference on Computer Vision and Pattern Recognition (CVPR)*, pp. 770–778. doi:10.1109/CVPR.2016.90.

- Hénaff, O.J., Srinivas, A., De Fauw, J., Razavi, A., Doersch, C., Eslami, S., Oord, A.v.d., 2019. Data-efficient image recognition with contrastive predictive coding. *arXiv preprint arXiv:1905.09272* .
- Hinton, G., Vinyals, O., Dean, J., 2015. Distilling the knowledge in a neural network. *stat* 1050, 9.
- Hou, L., Nguyen, V., Kanevsky, A.B., Samaras, D., Kurc, T.M., Zhao, T., Gupta, R.R., Gao, Y., Chen, W., Foran, D., et al., 2019. Sparse autoencoder for unsupervised nucleus detection and representation in histopathology images. *Pattern Recognition* 86, 188–200.
- Hu, B., Tang, Y., Eric, I., Chang, C., Fan, Y., Lai, M., Xu, Y., 2018. Unsupervised learning for cell-level visual representation in histopathology images with generative adversarial networks. *IEEE Journal of Biomedical and Health Informatics* 23, 1316–1328.
- Kather, J.N., Halama, N., Marx, A., 2018. 100,000 histological images of human colorectal cancer and healthy tissue. URL: <https://doi.org/10.5281/zenodo.1214456>, doi:10.5281/zenodo.1214456.
- Kingma, D.P., Ba, J., 2014. Adam: A method for stochastic optimization. *arXiv preprint arXiv:1412.6980* .
- Komura, D., Ishikawa, S., 2018. Machine learning methods for histopathological image analysis. *Computational and structural biotechnology journal* 16, 34–42.
- Li, J., Yang, S., Huang, X., Da, Q., Yang, X., Hu, Z., Duan, Q., Wang, C., Li, H., 2019. Signet ring cell detection with a semi-supervised learning framework, in: *International Conference on Information Processing in Medical Imaging*, Springer. pp. 842–854.
- Martel, A.L., Nofech-Mozes, S., Salama, S., Akbar, S., Peikari, M., 2019. Assessment of residual breast cancer cellularity after neoadjuvant chemotherapy using digital pathology [data set]. <https://doi.org/10.7937/TCIA.2019.4YIBTJNO>.
- Mehra, R., et al., 2018. Breast cancer histology images classification: Training from scratch or transfer learning? *ICT Express* 4, 247–254.
- Mikolov, T., Chen, K., Corrado, G., Dean, J., 2013. Efficient estimation of word representations in vector space. *arXiv preprint arXiv:1301.3781* .
- Misra, I., Maaten, L.v.d., 2020. Self-supervised learning of pretext-invariant representations, in: *Proceedings of the IEEE/CVF Conference on Computer Vision and Pattern Recognition*, pp. 6707–6717.

- Nir, G., Hor, S., Karimi, D., Fazli, L., Skinnider, B.F., Tavassoli, P., Turbin, D., Villamil, C.F., Wang, G., Wilson, R.S., Iczkowski, K.A., Lucia, M.S., Black, P.C., Abolmaesumi, P., Goldenberg, S.L., Salcudean, S.E., 2018. Automatic grading of prostate cancer in digitized histopathology images: Learning from multiple experts. *Medical Image Analysis* 50, 167 – 180. URL: <http://www.sciencedirect.com/science/article/pii/S1361841518307497>, doi:<https://doi.org/10.1016/j.media.2018.09.005>.
- Noroozi, M., Favaro, P., 2016. Unsupervised learning of visual representations by solving jigsaw puzzles, in: *European Conference on Computer Vision*, pp. 69–84.
- Peikari, M., Salama, S., Nofech-Mozes, S., Martel, A.L., 2017. Automatic cellularity assessment from post-treated breast surgical specimens. *Cytometry Part A* 91, 1078–1087.
- Peikari, M., Salama, S., Nofech-Mozes, S., Martel, A.L., 2018. A cluster-then-label semi-supervised learning approach for pathology image classification. *Scientific reports* 8, 1–13.
- Ronneberger, O., Fischer, P., Brox, T., 2015. U-net: Convolutional networks for biomedical image segmentation, in: *International Conference on Medical image computing and computer-assisted intervention*, Springer. pp. 234–241.
- Russakovsky, O., Deng, J., Su, H., Krause, J., Satheesh, S., Ma, S., Huang, Z., Karpathy, A., Khosla, A., Bernstein, M., Berg, A.C., Fei-Fei, L., 2015. ImageNet Large Scale Visual Recognition Challenge. *International Journal of Computer Vision (IJCV)* 115, 211–252. doi:10.1007/s11263-015-0816-y.
- Schroff, F., Kalenichenko, D., Philbin, J., 2015. Facenet: A unified embedding for face recognition and clustering, in: *Proceedings of the IEEE conference on computer vision and pattern recognition*, pp. 815–823.
- Spanhol, F.A., Oliveira, L.S., Petitjean, C., Heutte, L., 2016. A dataset for breast cancer histopathological image classification. *Ieee transactions on biomedical engineering* 63, 1455–1462.
- Tajbakhsh, N., Shin, J.Y., Gurudu, S.R., Hurst, R.T., Kendall, C.B., Gotway, M.B., Liang, J., 2016. Convolutional neural networks for medical image analysis: Full training or fine tuning? *IEEE transactions on medical imaging* 35, 1299–1312.
- Tarvainen, A., Valpola, H., 2017. Mean teachers are better role models: Weight-averaged consistency targets improve semi-supervised deep learning results, in: *Advances in neural information processing systems*, pp. 1195–1204.

- Tian, Y., Krishnan, D., Isola, P., 2019. Contrastive multiview coding. arXiv preprint arXiv:1906.05849 .
- Veeling, B.S., Linmans, J., Winkens, J., Cohen, T., Welling, M., 2018. Rotation equivariant cnns for digital pathology, in: International Conference on Medical image computing and computer-assisted intervention, Springer. pp. 210–218.
- Veta, M., Heng, Y.J., Stathonikos, N., Bejnordi, B.E., Beca, F., Wollmann, T., Rohr, K., Shah, M.A., Wang, D., Rousson, M., et al., 2019. Predicting breast tumor proliferation from whole-slide images: the tupac16 challenge. *Medical image analysis* 54, 111–121.
- Wu, Z., Xiong, Y., Yu, S., Lin, D., 2018. Unsupervised feature learning via non-parametric instance-level discrimination. arXiv preprint arXiv:1805.01978 .
- Xu, J., Xiang, L., Liu, Q., Gilmore, H., Wu, J., Tang, J., Madabhushi, A., 2015. Stacked sparse autoencoder (SSAE) for nuclei detection on breast cancer histopathology images. *IEEE Transactions on Medical Imaging* 35, 119–130.
- Yakubovskiy, P., 2020. Segmentation models pytorch.
- You, Y., Gitman, I., Ginsburg, B., 2017. Large batch training of convolutional networks. arXiv: Computer Vision and Pattern Recognition .
- You, Y., Li, J., Reddi, S., Hseu, J., Kumar, S., Bhojanapalli, S., Song, X., Demmel, J., Keutzer, K., Hsieh, C.J., 2019. Large batch optimization for deep learning: Training bert in 76 minutes, in: International Conference on Learning Representations, p. 1.

Appendix A. Foreground filtering

Due to their immense size, WSIs contain many regions that may be irrelevant for histopathology, such as ink, creases, fat, and white background. We threshold each WSI in HSV color space, with the following threshold parameters: $0.65 > hue > 0.5$, $saturation > 0.1$, and $0.9 > value > 0.5$. The bounds are experimentally determined using a public breast cancer segmentation dataset (Aresta et al., 2019) to isolate the irrelevant background regions. Each WSI is tiled into patches of size 224×224 pixels, and patches with foreground ratios $\geq 50\%$ are used as unsupervised training data.

Appendix B. Datasets

Appendix B.1. Training datasets

Image Patch Datasets

Dataset	Organ	Resolution	Staining	Number of patches	Image Type
AML-Cytomorphology LMU	blood	100x	Wright's stain	18365	patch
andrewjanowczyk epi	breast	20x	H&E	125	patch
andrewjanowczyk lymphoma	various	40x	H&E	374	patch
andrewjanowczyk mitosis	breast	40x	H&E	311	patch
andrewjanowczyk nuclei	breast	40x	H&E	142	patch
andrewjanowczyk tubule	colorectal	40x	H&E	85	patch
bach part A	breast	20x	H&E	400	patch
BreakHis v1	breast	4, 10, 20, 40x	H&E	7909	patch
breastpathq	breast	20x	H&E	47345	patch
C-NMC training data	blood, bone	Unknown	H&E	10661	patch
CoNSeP	colon	40x	H&E	41	patch
CRCHistoPhenotypes	colorectal	20x	H&E	200	patch
Pannuke Fold 1	various	various	H&E	2656	patch
glas 2015	colon	20x	H&E	165	patch
icpr2014	breast	20, 40x	H&E	3975	patch
icpr 2012	breast	40x	H&E	100	patch
lyon2019	breast, colon, prostate	40x	anti CD3, CD8	441	patch
MiMM SBILab	bone	100x	Jenner- Giemsa	85	patch
MoNuSeg Training Data	Various	40x	H&E	30	patch
NCT-CRC-HE-100k	liver, colorectal	20x	H&E	107180	patch
Prostate-MRI	prostate	Unsure	H&E	26	patch
ramtab	colon	unsure	various fluorescence	200	patch
SN-AM B-ALL and MM	blood, bone	100x	Jenner-Giemsa	61	patch
TNBC NucleiSegmentation	breast	40x	H&E	50	patch
warwick beta cell dataset	pancreas	40x	H-DAB	20	patch

Whole-Slide Datasets

Dataset	Organ	Resolution	Staining	Number of WSIs	Image Type
TCGA-BLA	bladder	40x	H&E	469	WSI
TCGA-BRCA	breast	20, 40x	H&E	1987	WSI
TCGA-CESC	cervix	40x	H&E	327	WSI
TCGA-COAD	colon	20, 40x	H&E	983	WSI
TCGA-ESCA	esophagus	20, 40x	H&E	260	WSI
TCGA-GBM	brain	20, 40x	H&E	1193	WSI
TCGA-HNSC	head, neck	20, 40x	H&E	791	WSI
TCGA-KICH	kidney	20, 40x	H&E	275	WSI
TCGA-KIRC	renal	20, 40x	H&E	1656	WSI
TCGA-KIRP	renal	20, 40x	H&E	475	WSI
TCGA-LGG	brain	40x	H&E	728	WSI
TCGA-LIHC	liver	20, 40x	H&E	492	WSI
TCGA-LUAD	chest	20, 40x	H&E	1067	WSI
TCGA-LUSC	lung	20, 40x	H&E	1100	WSI
TCGA-OV	ovary	20x	H&E	1376	WSI
TCGA-PRAD	prostate	20, 40x	H&E	736	WSI
TCGA-READ	rectum	20, 40x	H&E	364	WSI
TCGA-SARC	various	20, 40x	H&E	290	WSI
TCGA-STAD	stomach	20, 40x	H&E	771	WSI
TCGA-THCA	thyroid	20, 40x	H&E	639	WSI
TCGA-UCEC	uterus	20, 40x	H&E	805	WSI
CPTAC-AML	marrow, blood	40x	PAS, Wright	123	WSI
CPTAC-CCRCC	kidney	20x	H&E	783	WSI
CPTAC-CM	skin	20x	H&E	402	WSI
CPTAC-GBM	brain	20x	H&E	508	WSI
CPTAC-HNSCC	head, neck	20x	H&E	390	WSI
CPTAC-LSCC	lung	20x	H&E	1073	WSI
CPTAC-LUAD	lung	20x	H&E	1065	WSI
CPTAC-PDA	pancreas	20x	H&E	557	WSI
CPTAC-UCEC	uterus	20x	H&E	887	WSI
bach wsi	breast	20x	H&E	30	WSI
camelyon16	lymph node	40x	H&E	400	WSI
tupac16	breast	40x	H&E	821	WSI
camelyon17	lymph node	40x	H&E	1000	WSI
SLN-Breast	breast	20x	H&E	130	WSI

Table B.13: Datasets used for pretraining models.

Appendix B.2. Validation datasets

For all validation datasets, training data is comprised of 50% of total data, with 25% for both validation and testing sets, unless otherwise mentioned. For classification, we used the following five datasets: BACH challenge data (Aresta et al., 2019), Patch Camelyon (Veeling et al., 2018), BreakHis (Spanhol et al., 2016), NCT-CRC-HE-100K (Kather et al., 2018), and PANDA (Bulten et al., 2020).

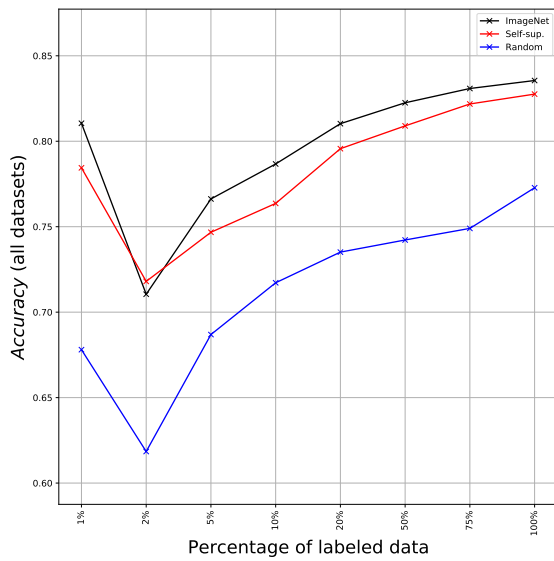
The BACH classification dataset contains 400 patches of size 2048×1536 pixels extracted from breast biopsy WSIs. The dataset is evenly split into four classes (normal, benign, in situ carcinoma, and invasive carcinoma), and the challenge task was to automatically classify images into these classes. The Patch Camelyon dataset contains 327680 image patches with size 96×96 taken from whole-slide scans of lymph node sections. Each image in the dataset is labelled with a positive or negative class, with the positive label denoting that the center 32×32 pixels of the image contains metastatic tissue. The BreakHis dataset contains 7909 patches of size 700×460 pixels taken from WSIs of breast tumor tissue. The data is labelled as either benign or malignant, and images belong to one of four magnifying factors (40x, 100x, 200x, and 400x). The NCT-CRC-HE-100K dataset contains 107180 patches of size 224×224 pixels. The split differs for this dataset, with 75000 patches in the training set, 25000 in validation, and 7180 in the test set. The test set comes from a related dataset called CRC-VAL-HE-7K, which was recommended for use as validation for the larger dataset. Images are taken from 86 stained colorectal cancer tissue slides. The data is split into seven classes: Adipose (ADI), background (BACK), debris (DEB), lymphocytes (LYM), mucus (MUC), smooth muscle (MUS), normal colon mucosa (NORM), cancer-associated stroma (STR), and colorectal adenocarcinoma epithelium (TUM). The PANDA challenge dataset contains 11000 WSIs of prostate tissue biopsies. The challenge task is to correctly classify whole-slides based on slide-level ISUP grades ranging from 0 to 5. The challenge organizers also provide a segmentation label mask for the majority of WSIs from a particular image provider (Radboud University Medical Center) to show which areas of the slide lead to the final ISUP grade. These masks contain 6 classes: background, stroma, benign epithelium, Gleason 3, Gleason 4, and Gleason 5. To make the dataset more manageable, we extracted a total of 151278 patches of size 1024×1024 by labelling each image patch according to the majority segmentation class given in the train label masks provided.

For segmentation, we used the following three datasets: BACH challenge dataset (Aresta et al., 2019), Gleason2019 (Nir et al., 2018), and DigestPath2019 (Li et al., 2019). The BACH segmentation dataset originates from part B of the challenge, and consists of 10 breast biopsy WSIs with pixel-level segmentation masks. These whole-slides are split 5/3/2 for train/validation/test respectively. The segmentation labels are

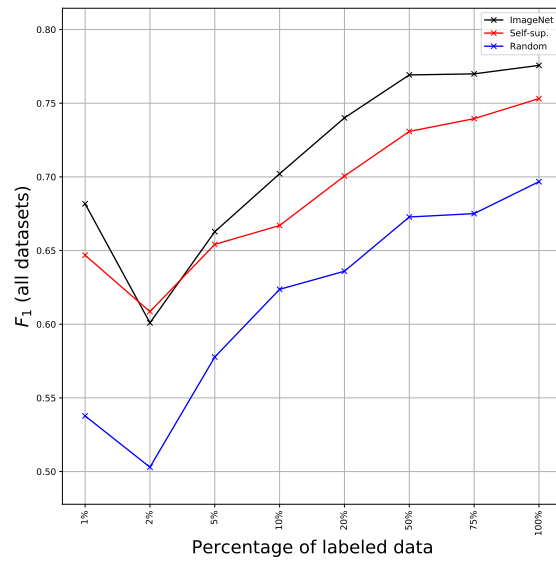
the same 4 classes in the classification dataset. Patches of size 1024×1024 pixels were extracted from each slide with a sliding window. The Gleason2019 dataset contains 244 tissue micro-array (TMA) images from prostate biopsies. The segmentation labels for this dataset are the Gleason scores for each pixel in the image, ranging from 1 (healthy) to 5 (abnormal). The DigestPath2019 challenge dataset contains 250 5000×5000 pixel image patches taken from colonoscopy tissue slides. For our task, we resize each patch and its corresponding pixel-level label image to 1024×1024 . The segmentation masks provided for this dataset are divided into two classes (benign or malignant), and the aim of this challenge is to use these segmentation labels to identify early-stage colon tumors.

For regression, we used the BreastPathQ dataset (Akbar et al., 2019). It consists of a total of 2579 patches with size 512×512 pixels extracted from 69 WSIs of Post-NAT-BRCA specimens (Peikari et al., 2017). BreastPathQ images are labelled according to the percentage of cancer cellularity in each patch.

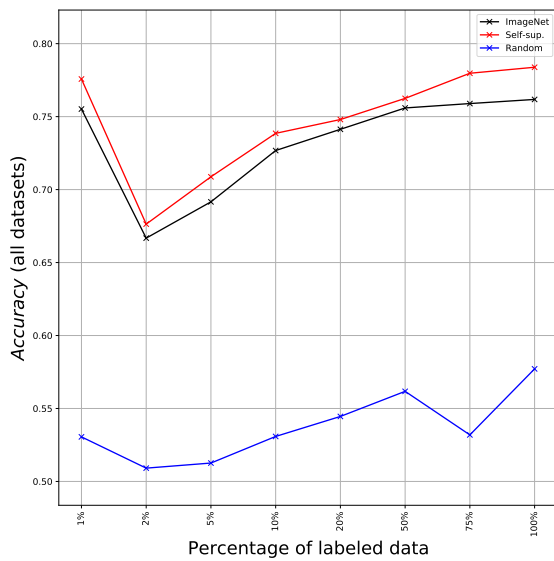
Appendix C. Classification results for Resnet 34, 50, and 101



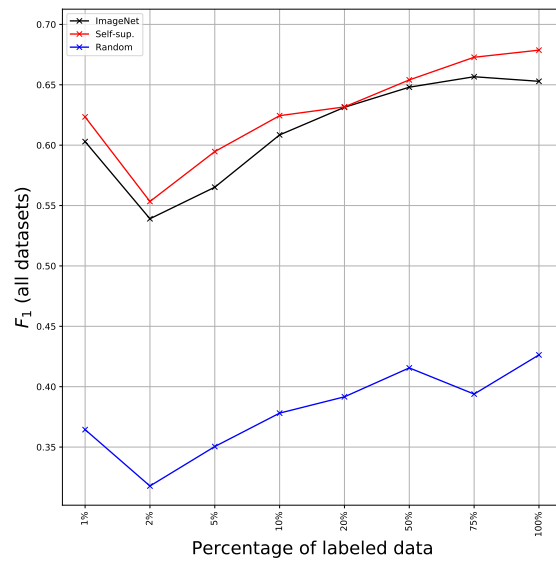
(a) Accuracy (fine tuning)



(b) Macro F_1 (fine tuning)



(c) Accuracy (last layer)



(d) Macro F_1 (last layer)

Figure C.10: Average classification performance for both fine tuning and last layer settings on five datasets for the pretrained Resnet 34 model.

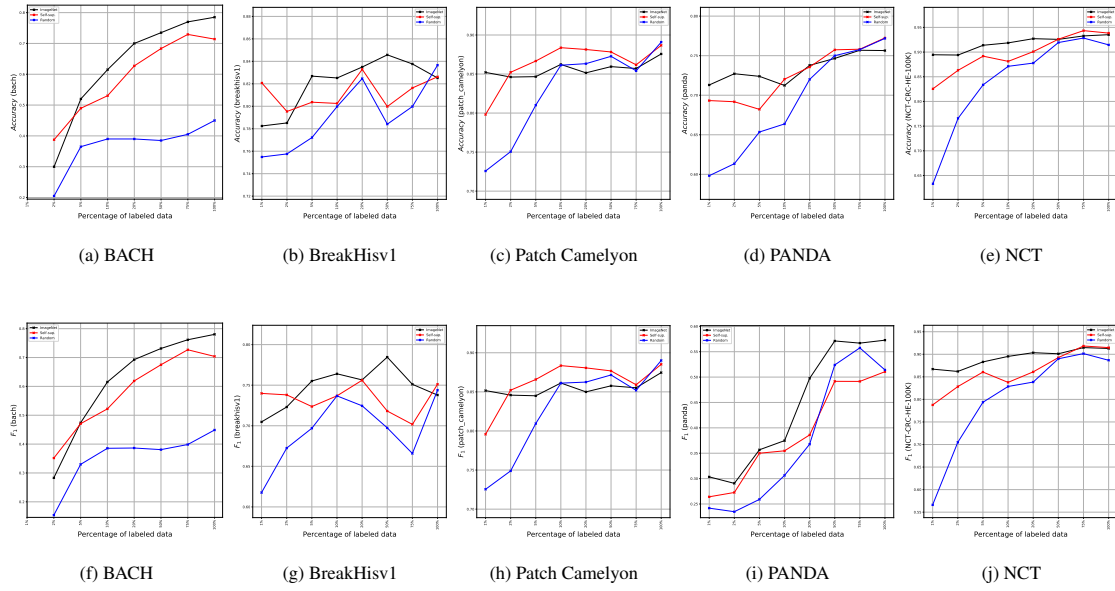


Figure C.11: Classification performance for fine tuning setting on five datasets for the pretrained Resnet 34 model.

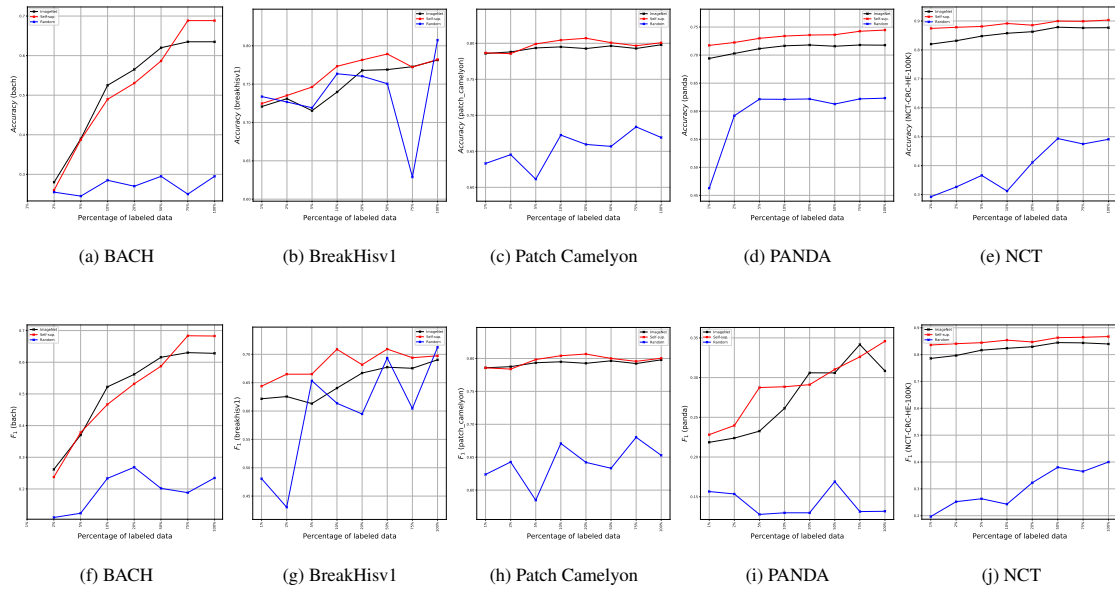
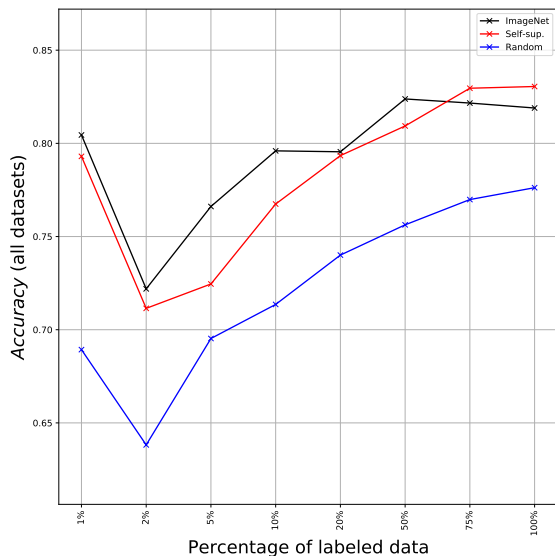
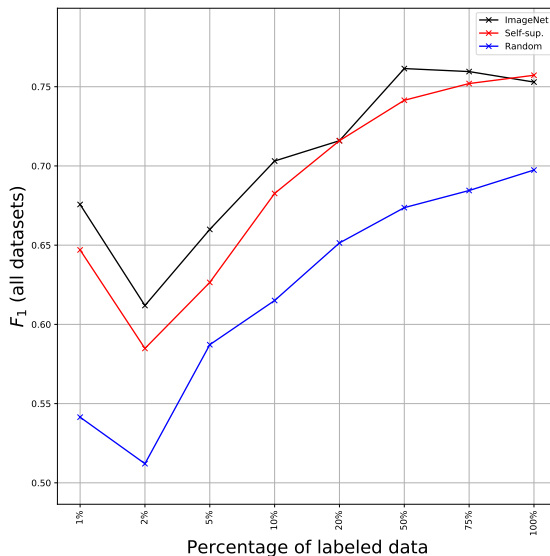


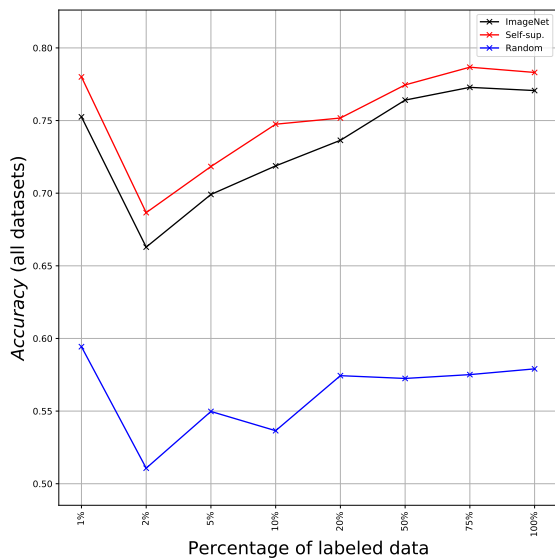
Figure C.12: Classification performance for last layer setting on five datasets for the pretrained Resnet 34 model.



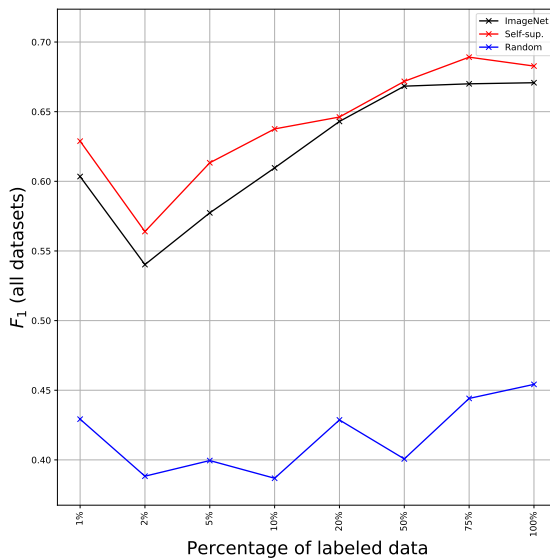
(a) Accuracy (fine tuning)



(b) Macro F_1 (fine tuning)



(c) Accuracy (last layer)



(d) Macro F_1 (last layer)

Figure C.13: Average classification performance for both fine tuning and last layer settings on five datasets for the pretrained Resnet 50 model.

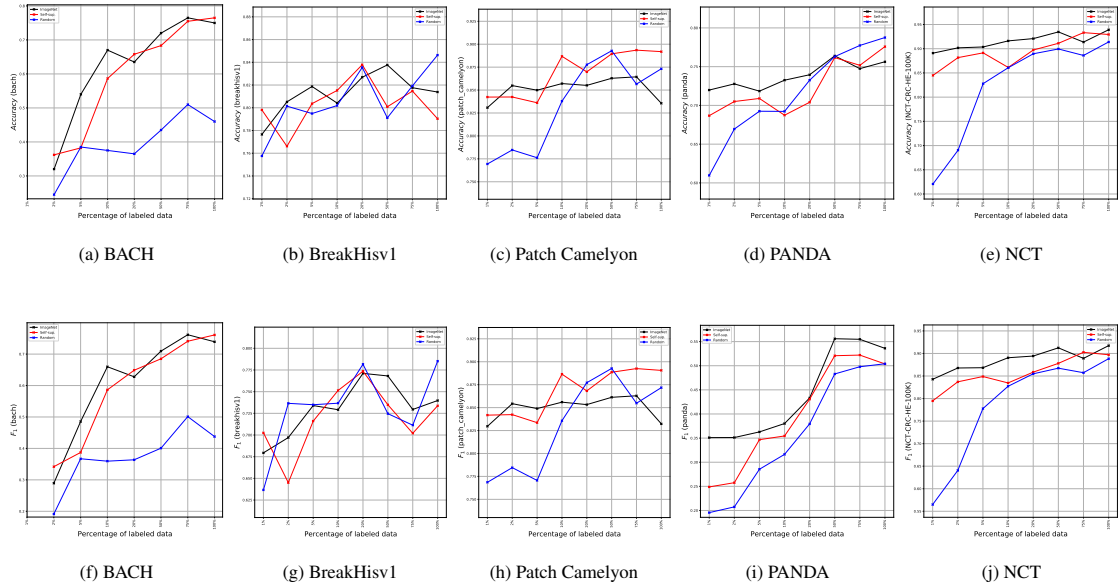


Figure C.14: Classification performance for fine tuning setting on five datasets for the pretrained Resnet 50 model.

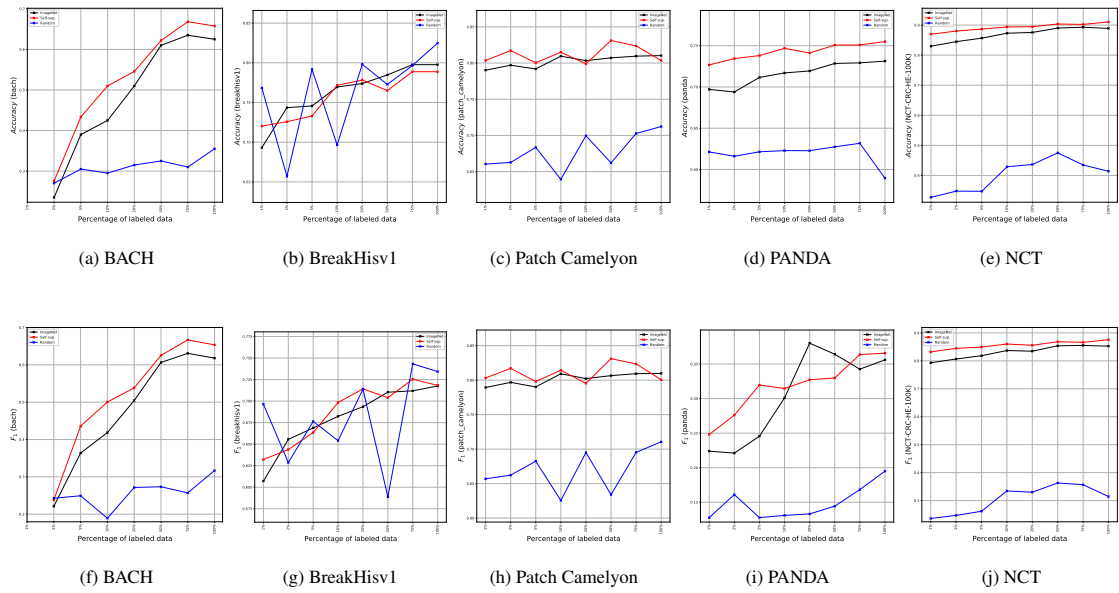
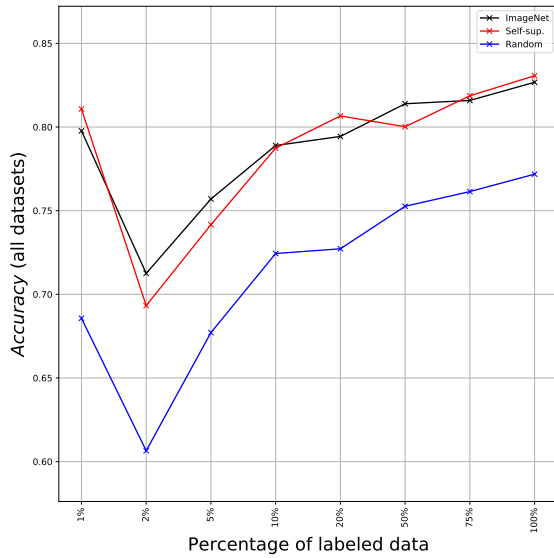
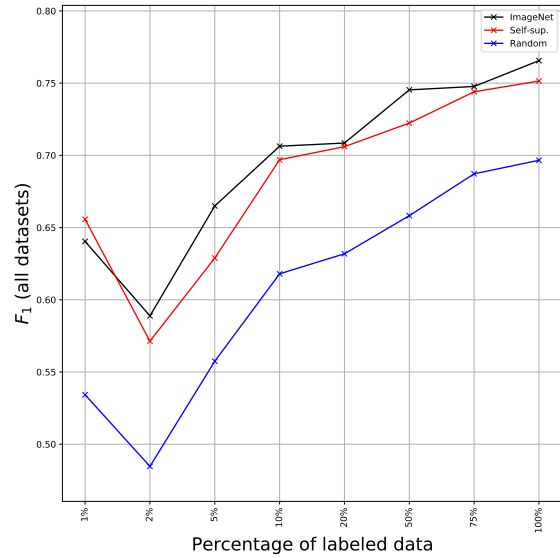


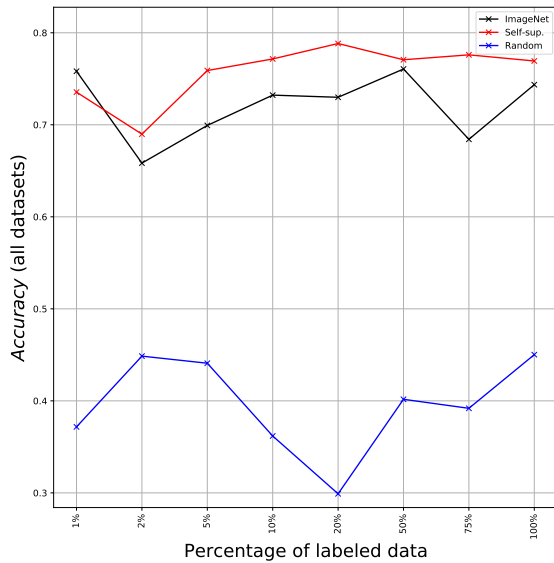
Figure C.15: Classification performance for last layer setting on five datasets for the pretrained Resnet 50 model.



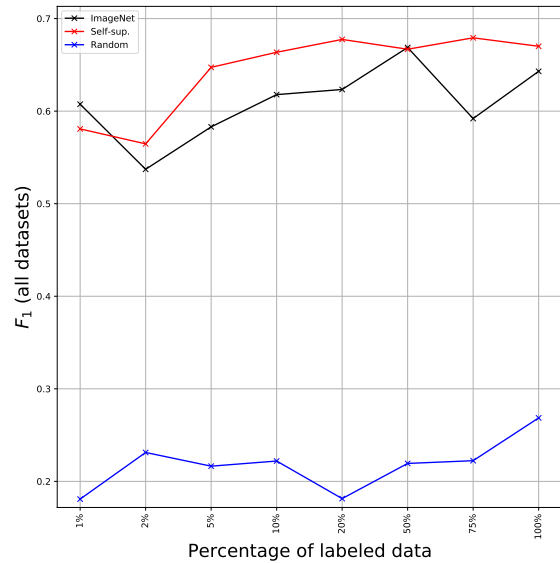
(a) Accuracy (fine tuning)



(b) Macro F_1 (fine tuning)



(c) Accuracy (last layer)



(d) Macro F_1 (last layer)

Figure C.16: Average classification performance for both fine tuning and last layer settings on five datasets for the pretrained Resnet 101 model.

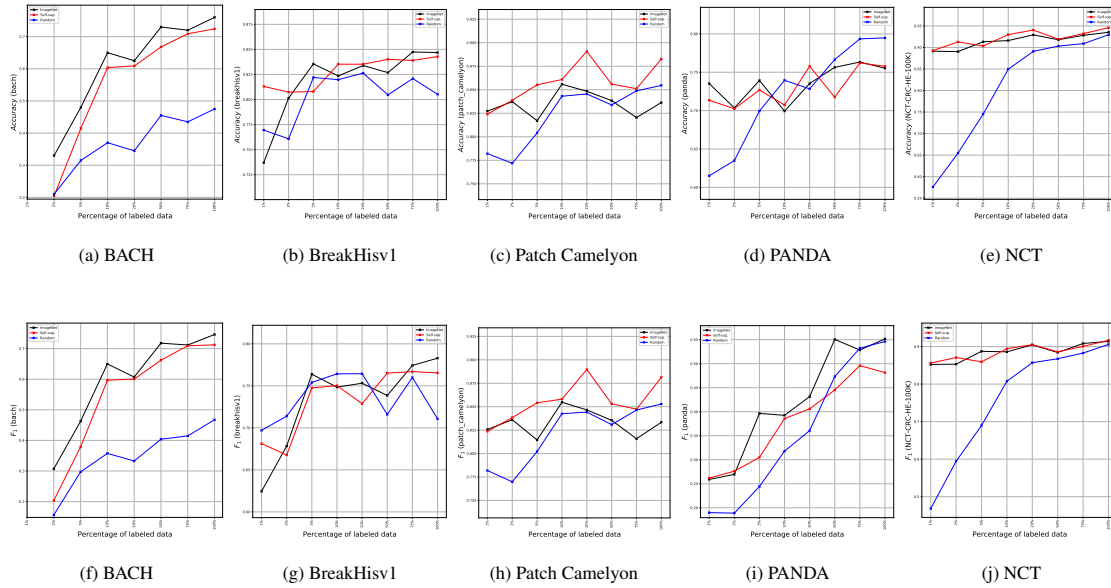


Figure C.17: Classification performance for fine tuning setting on five datasets for the pretrained Resnet 101 model.

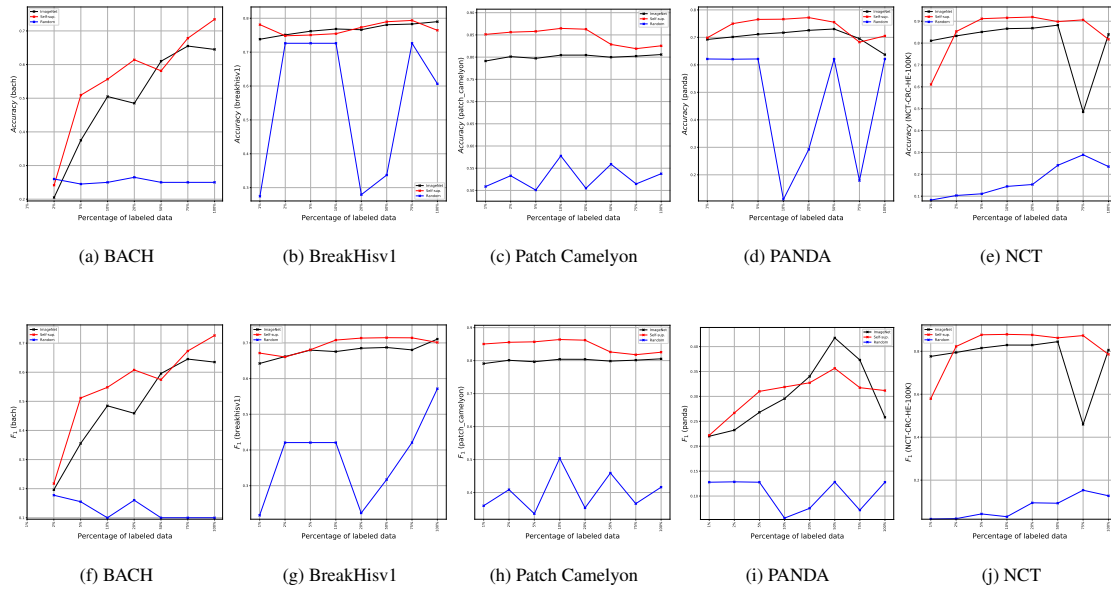


Figure C.18: Classification performance for last layer setting on five datasets for the pretrained Resnet 101 model.